METALLURGICAL LENGTH PREDICTION IN CONTINUOUS CASTING

by

Rashed Daoud Al Manasir

A Thesis

Submitted to the Faculty of Purdue University

In partial Fulfillment of the Requirements for the degree of

Master of Science in Mechanical Engineering

Department of Mechanical and Civil Engineering

Hammond, Indiana

May 2023

THE PURDUE UNIVERSITY GRADUATE SCHOOL
STATEMENT OF COMMITTEE APPROVAL

Dr. Chenn Q. Zhou, Chair

Department of Mechanical and Civil Engineering

Dr. Yun Liu

Department of Mechanical and Civil Engineering

Dr. Xiuling Wang

Department of Mechanical and Civil Engineering

Approved by:

Dr. Xiuling Wang

This work is devoted to my family and my friends whom despite the challenges of life, always support me in all that I do.

ACKNOWLEDGMENTS

The members of the Steel Manufacturing Simulation and Visualization Consortium (SMSVC) deserve credit for funding this study. The members of the project's Technical Committee (PTC) deserve special recognition for their dedication to the project's success. Thanks to the help of the Center for Innovation through Visualization and Simulation (CIVS), this work was able to be completed. With their many initiatives, CIVS has helped me develop as a researcher, engineer, and person. They were essential in shaping me and bringing forth dormant skills on my part. CIVS has helped me develop in numerous ways, including as a communicator, presenter, manager, and people person. Thank you for allowing me to explore my potential here at CIVS.

I would like to thank both advisors, Professor Armin Silaen and Professor Chenn Q. Zhou. Mainly, the former for the guidance and teaching and the latter for the resources and influence. Professor Armin helped me reshape and remold my technical abilities and my leadership skills, he surely was one of the few role models one can encounter in life and record the lessons he learns from. He taught me how to simplify complexity and work smart, made me a better person with every encounter and every weekly meeting we had. But most importantly, he taught me how to lead by example and actions rather than words. We have had our own internal arguments in which I have consistently lost, but despite knowing that I was only being obstinate and obnoxious, he was modest and humble enough to allow me to express myself. He is strict but fair, he was also sensible enough to permit me to do it because he understood that it is the only way to examine the idea of creativity and its significance in today's engineering industry. I owe so much of who I am becoming as an engineer, a thinker and a philosopher to the guidance of this man and his leadership. His teachings will forever be imprinted into my personality. As for Professor Chenn Q. Zhou, I learned so much from her goal-oriented, energetic and persevering personality. Her emphasis on being timely mannered and following a certain plan are some good skills I was lacking and found so much to learn from. Her support in terms of providing opportunities and resources for us to learn is something one can the least be grateful for, she was indeed a good provider of opportunity and skills that will forever be remembered. I would also like to appreciate my other committee members, Professor Yun “Tom” Liu and Professor Xiuling Wang. They had a significant role in

my achievement at Purdue. They not only reviewed my thesis but also the course work I completed with their instruction, which served as a stepping stone to my accomplishment.

Moreover, I want to thank Kyle Toth, Professor Tyamo Okosun, and Nick Walla for their assistance in completing my project, whether in a direct or indirect ways, I am forever grateful. Also and in a very special way, I would like to thank my colleagues. Words alone cannot adequately express my gratitude for their outstanding contributions and the positive influences they had on my life, especially the likes of Sushma Sanisetty, Ninad Patil, John Rosser, Saswot Thapa, Neel Busa, Emran Syed, Pavan Vimula, Anurag Karambalekar, Misbahuddin Syed, Samuel Neilson, Mingqian Wang, Vitalis Anisiuba, Uzor Chukwunedum, Ogochukwu Oduruihe, Joel Godinez, Xipeng Guo and of course Haibo Ma. They made some useful impact towards my project and my stay at Purdue.

To my dear family as well, I owe a big part of my achievement. They have been forever supportive of my vision and beliefs, especially the love my life, my mom. My father and my siblings were also a support system that one can best describe it as too good to be true. To my second family back home, the Rosary sisters school family, I owe a lot of this academic achievement and much more of my morality to the teachings and education I had at such a loving place. The University of Jordan, its professors and to the generous and humble people of Jordan, this would have never been accomplished without you. Jordan as a holistic entity was one of the biggest reasons I made it this far and the least I can say and do is represent such a beautiful and ancient civilization the best way I find possible. Last but not least, if it was not for the guidance of God, the most compassionate and the most merciful, my whole identity would be nothing. To him I surrendered myself and indeed, his promise was true and my prayers were always answered. I thank him for guiding me along each and every path of my life even with all my wrongdoings, for he is indeed the most compassionate and the most merciful.

TABLE OF CONTENTS

LIST OF FIGURES

NOMENCLATURE

St	Stoke's number
Φ_v	dispersed phase volume
Φ_m	mass loading
ϵ	mean turbulent kinetic energy
τ_p	particle response time
τ_n	flow time scale
η	Kolmogorov scale
d	particle density
ρ_f	fluid density
ρ_p	particle density
Fr	Froude number
a_n	Kolmogorov acceleration
L	intact length
t_s	sheet thickness
We	weber number
Re	Reynold's number
u_R	relative velocity
ρ_l	liquid density
μ_l	liquid viscosity
σ	surface tension
u_l	liquid viscosity
D_l	central tube diameter
A_l	cross-sectional area for liquid
A_g	cross-sectional area for gas
μ_{drop}	droplet viscosity

Oh	Ohnesorge number
ρ_{air}	air density
σ_{drop}	droplet surface tension
d_{drop}	droplet diameter
h	heat transfer coefficient
q	heat flux
T_w	wall temperature
$S_{air\text{-}drop}$	source term
g	gravity
V_{cell}	cell volume
χ	composition field
Ω	maximum growth rate of wavy turbulence
Λ	dominance wavelength of wavy disturbances
T_{drop}	droplet temperature
T_R	radiation temperature
h_{fg}	latent heat of droplet
μ_{air}	air density
C_D	drag coefficient
x_{drop}	droplet position vector
σ_{SB}	Stefan-Boltzmann constant
ε_{drop}	droplet emissivity
c_p	specific heat of droplet
C_s	concentration of the vapour at droplet surface
C_ω	concentration of the vapour in the bulk flow
Ψ	the impinge angle on the horizontal plane
H_π	sheet height at $\psi = \pi$
β_ω	k-ω SST turbulence model coefficient

β_k	k-ω SST turbulence model coefficient
m_{drop}	mass of droplet
ρ_{steel}	density of steel
k	turbulent kinetic energy
$\bar{\bar{\tau}}$	stress tensor
T_{liq}	liquidus temperature
T_{sol}	solidus temperature
f_{sol}	solid fraction
h_{lat}	latent heat release
u_{steel}	velocity of steel
$u_{stationary}$	velocity of the stationary reference frame
u_{moving}	velocity of the moving reference frame
u_r	relative velocity between the stationary and moving reference frames
$V_{casting}$	casting speed
$D_{standoff}$	standoff distance
Q_{water}	water flow rate
P_{air}	air pressure

ABSTRACT

A thorough analysis of spraying situations was carried out in the pursuit of having an appropriate spread and mapping for the spraying system in the continuous casting process. For each spray and each section, CFD simulations were utilized to analyze all potential spraying conditions while moving over the continuous steel caster. It was necessary to thoroughly examine the distribution of heat transfer coefficient (HTC) along the caster, therefore variables such overlap, stand-off distance, water flow rate, spray angle, and casting speed were taken into consideration. A flat fan atomizer model was used to simulate this distribution and its impact, and different spraying scenarios were run. More research was done on the effects of each separate spray on HTC, paying particular attention to the overlap phenomena. By simply entering the HTC data for each spray simulation and its corresponding coordinates, as well as stitching those profiles into multiple profiles that fit into its further corresponding segment, an assembly for each of these scenarios unto each segment along the full caster was also accomplished using MATLAB. Further MATLAB code was built to "bend" the coordinates of the profiles in accordance with the bend or curve of the caster, which was also taken into consideration. The study's primary focus when it came to the solidification model's next component was rebuilding the caster geometry. To measure and examine the shell thickness, surface temperature, and many other phenomena along the casting, numerous "straight" segments were previously employed. The caster's curvature was considered in the newly revised design, along with changes to the extracting technique used for many other phenomena in general and shell thickness in particular. This is done in order to create a more realistic design that mimics the caster's actual shape and the physics that affect it. Also, a successful integration of the two projects stated above was accomplished, and parametric studies were also carried out, including a study of the impact of casting speed and nozzle clogging on metallurgical length. In order to model the actual process of casting, the steel’s temperature-dependent material properties were studied using the thermodynamic software JMatPro. For the research of the flat fan atomizer model, the ANSYS Fluent 2020R1 CFD tool was heavily utilized, and for the investigation of the solidification of steel, the STARCCM+ CFD program. The MATLAB R2018a software was used to map the curved Heat Transfer Coefficient (HTC) profiles, straighten such curved data, and visualize the shell expansion by extracting curved coordinates. The results of this study can be used to enhance continuous casting procedures and optimization.

1. INTRODUCTION

1.1 Continuous casting overview

The continuous casting (CC) process is used to produce more than 90% of the steel in the world, which emerged as a technology in the late 1950s and relies heavily on secondary cooling [1,2]. In 2009, the world produced more than 1220 million tons of crude steel, with 92% of that coming from continuously cast steel [3]. So, the importance of spray cooling in this and many other processes where it is involved becomes clear. The continuous casting method is depicted in Figure 1-1.

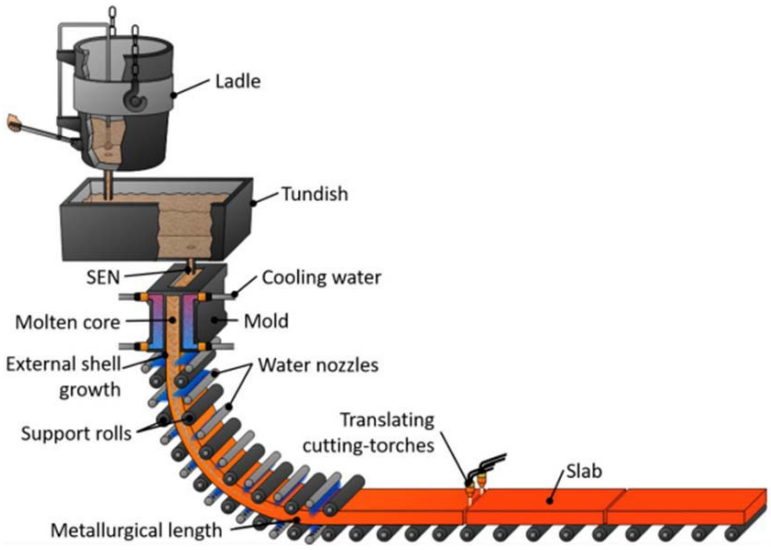

Figure 1-1: Continuous casting process [4]

After being cooled to about 1200 degrees Celsius (1473 degrees Fahrenheit), a shell made of steel CC emerges from the mold. The strand then travels through the secondary cooling system, which is a containment spray cooling arrangement with closely spaced support rollers and interspersed nozzles to guarantee full solidification over its thickness. About 60% of the heat drained via this system comes from the secondary cooling system of CC machines (i.e., direct spray impingement, roll contact, radiation, and convection to draining water), albeit this contribution may be significantly bigger in its upper zones [5,6].

1.2 Motivations and Objectives

Around 98% of the crude steel produced in the United States goes through the CC process, in which a water-cooled mold is used to solidify molten steel using water sprays to create semi-finished slabs or billets. The quality of both the exterior and inside of the slab is directly related to the rate at which it is cooled, making secondary cooling a difficult process. The heat must be removed efficiently without causing the slab to crack or deform in any way. Low grade steel is produced because of inadequate spray cooling and solidification, which leads to flaws like cracking and breakout. Real-time online dynamic casting control systems are becoming increasingly popular in continuous casting as a means to increase yield and energy efficiency. These systems are built to reliably produce high-quality steel products via real-time temperature measurements and dynamic adjustment of the spray cooling rate. For real-time heat transfer and solidification calculations in the field, the key challenge is determining an accurate Heat Transfer Coefficient (HTC) for the steel product's surface. The correlations for predicting the spray cooling rate empirically have been developed with great care.

Nevertheless, these correlations are only valid under specific application circumstances. Building it takes a significant amount of time and effort, and there is no assurance that the correlation will continue to accurately predict HTC even if the development process is modified in any way. An in-depth investigation into the heat transfer mechanisms that take place during the secondary cooling step of continuous steel casting is required in order to achieve control and optimization goals for this step. The non-optimized solidification process also contributes to the formation of inhomogeneous steel properties. The project required the application of computational fluid dynamics modeling techniques so that the casting process could be regulated and improved upon. Simulation of droplet formation, droplet transport, and impingement heat transfer during secondary cooling with an air-mist nozzle in a 3D computational fluid dynamics (CFD) model is going to be done in this study with the intention of generating a multivariable correlation that can accurately predict the lumped HTC under any casting condition. This will be accomplished by using the model. It modeled the solidification of the whole continuous caster by taking into consideration the impacts of roll gap, roll diameter, casting speed, and superheat in order to estimate the metallurgical length and slab temperature. This was done in order to calculate the metallurgical length.

1.3 Simulation Software

Computational fluid dynamics (CFD) involves the use of numerical techniques and algorithms to evaluate fluids in several phases during both responding and non-reacting flows, with varying degrees of complexity in terms of thermodynamics, heat transfer, turbulence, and chemical reactions. Engineering, mathematics, and computer science are just few of the fields that contribute to the development of a CFD model that is both accurate and representative. Predictive uses for simulations include exploring what would happen in hypothetical situations that would be too risky or expensive to try out in real life, exploring how a process would scale, modeling the effects of potentially dangerous situations, and regulating and optimizing existing procedures. The conservation of mass, momentum, and energy are the three foundational governing equations of fluid dynamics. Developing an internal algorithm to calculate physical phenomena within a caster would be time expensive due to the complex nature and physics of solidification. Thus, it is best to use a professional CFD program such as ANSYS, Star-CCM+, or COMSOL. ANSYS Fluent 2021 R1 (ANSYS Inc., Pittsburgh, PA, USA) was used to conduct the air-mist spray investigation due to its well-deserved reputation for advanced physics modeling capabilities and market-leading precision in fluid simulation software. The STAR CCM+ software (Siemens Digital Industries Software, Plano, Texas, USA) was utilized to analyze steel solidification because of its sophisticated solidification modeler, superior mesh choices, and simple table-based data manipulation. MATLAB software (Mathworks, Natick, Massachusetts, USA) was used for assembling and mapping multiple Heat Transfer Coefficient (HTC) profiles from various spray simulation scenarios, plotting the shell growth by extracting curved coordinates and straightening such curved data and mapping the curved HTC profiles.

2. LITERATURE REVIEW

2.1 Spray cooling process

2.1.1 Heat exchange on the steel slab's surface

Many industrial applications use rapid jet cooling to transfer heat efficiently. By injecting liquid or gaseous flow at a particular distance against a heated surface, forced convection or boiling can produce high cooling rates. Jet impingement heat transfer cools semi-solidified moving slabs in continuous casting, runout tables in hot mill processes, gas turbine blades, electronic components, combustion engine walls, nuclear power plants, and other industrial processes. Impinging jet cooling has two regions: free jet and impingement heat transfer. In the free jet zone, cooling fluid from a nozzle creates a free submerged jet with an undisturbed potential core in the middle surrounded by a high-gradient shear layer, where momentum and energy transfer occur. At the stagnation point, the jet becomes a wall jet moving laterally parallel to the hot surface. Cooling fluid absorbs heat from the heated surface while moving outward, and the boiling regime gradually develops from induced convection in a single phase to transition boiling, film boiling, and nucleate boiling as wall superheat increases [7]. Jet impingement cooling performance depends on nozzle type, exit opening shape, number of phases, cooling fluid type and flow rate, jet direction, surface temperature and roughness, jet-to-surface distance, and jet-to-jet spacing [8-11].

Spray cooling causes surface temperature fluctuations on the solid shell in the secondary cooling region. Temperature differences can cause complex phase change and residual thermal stress in the steel slab. Undercooling and overcooling in the secondary cooling region greatly impair slab quality and process smoothness, making uniform cooling without cracking or deformation crucial [12]. Insufficient heat transfer across the cooling surface will cause breakout, where molten steel breaks the thin shell and bursts out. Due to thermal loads and strains, excessive cooling causes cracks and other problems [13].

The atomization process as well as the droplet-steel impingement heat transfer are the primary foci of the numerical simulation. In this model, the fragmentation of the water jet is not considered to be part of the process; nevertheless, the droplets that come from the disintegration of the jet are trailed in the frame of the length of the breakdown. Integrating Newton's second law allows one

to address the problem of droplet motion. In the Eulerian modeling framework, the air entrainment that occurs as a result of the hot steel slab and high-speed water injection as continuous phases.

For the production of steel of superior quality and increased tensile strength, the spray cooling rate in the secondary cooling region needs to be meticulously planned out and managed. Instead, a temperature field with an uneven distribution within the shell after it has been cemented can result in persistent thermal strains and stresses that eventually cause cracking and other flaws [24] [25].

Nevertheless, when casting is done continuously, it is impossible to gauge the temperature distribution within the solidified steel. An additional method known as HTC was suggested for use on the steel surface in order to assess the level of spray cooling and its homogeneity. From the perspective of heat transfer, Newton's law of cooling can be used to derive HTC, which states that:

$$q''_{total} = q''_{cond} + q''_{r} = \mathrm{HTC}\left(T_{face} - T_{spray}\right) + q''_{r} \quad (1)$$

<u>Continuous Phase</u>

The air phase is modeled with the steady-state Reynolds-Averaged Navier-Stokes (RANS) equations, tracking mass, momentum, and energy. The transition from water droplets to water vapor in the gaseous phase is handled with species transport. Only energy transport is solved for the solid steel material, tracking primary modes of heat transfer. [14]:

$$\nabla.\left(\rho_{air}\,\vec{u}_{air}\,\varphi - \Gamma_{\varphi}\nabla_{\varphi}\right) = \mathrm{S}_{\varphi} + \mathrm{S}_{\mathrm{drop-air}} \quad (2)$$

Where φ is a universal variable that represents one in mass, momentum, energy, and species transport equations. Sφ represents the universal variable. $S_{\text{drop-air}}$ describes droplet-air interaction. Unsteady droplet tracking follows air governing equations. Newton's law of motion integrates droplet motion from each computing cell's air velocity. The external source term incorporates droplet mass, momentum, and energy changes into air computations after each time step.

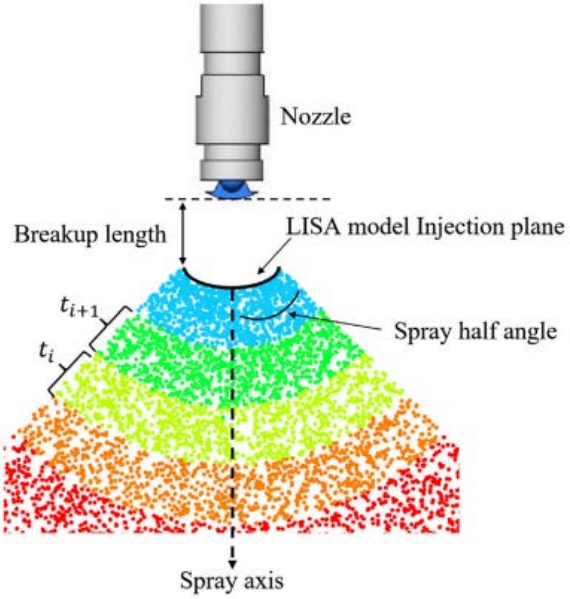

Figure 2-1: Droplet generation by LISA model [11]

The turbulence kinetic energy and particular turbulence dissipation rate are solved by the k-Shear Stress Transport (SST) turbulence model. This model was selected because it makes highly accurate predictions about the presence of vortices at the spray boundary and the separation of the flow on the steel surface without consuming a lot of computer resources. The model uses a blending function to transition between the two models by taking advantage of the k-model in most of the region and the k-model in the vicinity of walls [11] [15].

Discrete Phase

Droplet Formation

Physically, two consecutive steps lead to the formation of droplets: the dissolution of the liquid sheet and the dissolution of the ligaments.

Primary breakup is the term used to describe both breakdown processes, as opposed to secondary breakup, which happens when primary broken-up droplets fragment further as a result of aerodynamic instability or droplet-droplet collisions. The primary breakdown is a well-researched phenomenon, and in recent decades, the relevant hypotheses have undergone rigorous validation. [16] [17].

This work uses the LISA model to estimate droplet formation at the breakup length without recreating the primary breakup process or the internal flow inside the nozzle.

Figure 2-1 demonstrates the droplet production and injection process used in this study. The liquid jet released from a nozzle is a liquid sheet that breaks into ligaments and then droplets as a result of the development of minuscule wavy disturbances after traveling a certain distance (breakup length) from the nozzle's departure, according to the LISA model [18]. The most unstable disturbance determines the separation's length and its rate of increase:

$$L_b = \frac{U}{\Omega} \ln\left(\frac{\eta_b}{\eta_0}\right) \tag{3}$$

A set of droplets are delivered into the computational domain at the beginning of each droplet time step (ti) from a curved virtual injection plane that is situated below the nozzle exit by the disintegration length distance. According to the casting's operational state, the mass of water passing through the nozzle equals the overall mass of the inserted particles. On the injection plane, droplets are distributed at random, but their size distribution conforms to a Rosin-Rammler distribution with a spread number of 3.5. The diameter of the Rosin-Rammler distribution can be calculated using the following formula:

$$d_0 = 3.76 * \left(\frac{\pi\, C_L}{K_s}\right)\, (1 + 3Oh)^{1/6} \tag{4}$$

Droplet Motion

In the Lagrangian frame, each droplet time step's droplet motion is traced by solving Newton's law of motion.

$$\frac{d\,\vec{u}_{drop}}{dt} = \frac{3\,\mu_{drop}\, C_D Re_{drop}}{4\,\rho_{drop} d^2{}_{drop}} \left(\vec{u}_{air} - \vec{u}_{drop}\right) + \frac{\vec{g}\,(\rho_{drop} - \rho_{air})}{\rho_{drop}} \tag{5}$$

Under the supposition that a droplet maintains its spherical shape throughout its lifetime, the drag and gravitational forces govern the droplet's motion. The air-droplet interaction is represented by the drag coefficient (CD) and the drag force term, then can be computed using the piecewise function below [19].

$$C_D = \begin{cases} 0.424 & Re_{drop} > 1000 \\ \frac{24}{Re_{drop}} \left(1 + \frac{1}{6}\left(Re_{drop}\right)^{\frac{2}{3}}\right) & Re_{drop} \leq 1000 \end{cases} \tag{6}$$

To represent how turbulence in the gas phase causes droplet dispersion during atomization, the eddy-lifetime model is incorporated as well [20].

Droplet Temperature and Mass Change

A droplet transfers heat to the surrounding air as it moves through the gas phase. The amount of temperature change in a droplet is determined by energy conservation:

$$m_{drop}\, Cp\, \frac{dT_{drop}}{dt} = \pi d_{drop}^2 h \left(T_\infty - T_{drop}\right) + \frac{dm_{drop}}{dt}\, h_{fg} + \pi d_{drop}^2 \varepsilon_{drop} \sigma_{SB} \left(T_R^4 - T_{drop}^4\right) \quad (7)$$

The convective heat transfer coefficient h, can be obtained from the Ranz-Marshall model [21]

$$Nu_{drop} = \frac{h d_{drop}}{k_{air}} = 2.0 + 0.6 Re_{drop}^{0.5} Pr^{0.33} \quad (8)$$

The droplet mass is continually updated in each time step to simulate this process.

Droplet Breakup and Collision

Predictions of droplet collision and breakage are essential for the subsequent droplet-steel impingement heat transfer. The droplet sizes and numbers are significantly altered by these two occurrences. The WAVE breakdown model is used in this study to account for droplet breakup caused by the relative velocities of the surrounding air and the droplet. The jet instability theory and the model are comparable. The model predicts that the breakup time and size of a droplet are determined by the Kelvin-Helmholtz instability with the largest growth rate.

O'Rourke's algorithm is used to calculate the droplet-droplet collision [22]. Instead of determining whether the trajectories of two droplets collide, a technique is described that provides a stochastic estimate of collisions. If two droplets are in the same cell and the smaller droplet is located within the collision volume centered on the bigger one, they are deemed to be capable of colliding at each time step. As a cylinder, the collision volume is defined of length $(u1 - u2)\Delta t$ and circular area $\pi(r1 + r2)^2$. Where if the condition is met, the two droplets are destined to collide [11].

The trajectory offset between the smaller and larger droplets determines how a collision will turn out. The offset is calculated by the separation between the two drops and a collision-like random number [11].

Droplet-Steel Impingement Heat Transfer

Figure 4 illustrates the computation of droplet-steel impingement and heat transfer. The figure depicts a fluid cell, a solid cell, and a water droplet. The results are defined by the wall jet model and depend on the characteristics of the incoming droplet when a droplet enters a fluid cell next to a solid cell and impinges on the fluid-solid interface [11] [23].

Based on Ma, H., Silaen, A. K., & Zhou, C., Q. (2020), the impingement model takes three outcomes into account: deposit, reflection, and wall jet. After impingement, the droplet in the deposit mode remains on the steel surface and continues to absorb heat from the metal until it entirely evaporates. The vertical velocity component of droplet before impingement maintains same magnitude but a changes direction after impingement. The tangent velocity component's magnitude and direction remain the same [11].

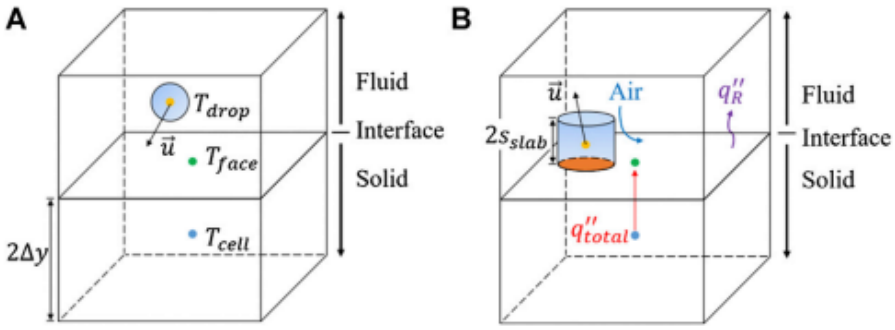

Figure 2-2: Droplet-steel impingement heat transfer calculation (A) before impingement, and (B) after impingement [11]

While a cluster of collision of closely spaced droplets with the steel surface to activate the wall jet mode. This constant flow of droplets loses its vertical component after impingement and becomes horizontal, mimicking an inviscid jet released from the surface's stagnation point. Figure 2-2 shows heat transfer between droplets and steel. Even though the droplet's lifetime sphericalness is assumed, the impact of droplet deformation is considered in the heat transfer calculation. The current work makes the assumption that a droplet impinges on a heated surface, transforms into a cylinder of equal capacity, and stays in touch with it for a brief moment.

Heat Transfer Coefficient Calculation

HTC is assessed following the completion of the simulation and during post-processing. In actuality, it is simpler to depict heat transfer by combining convection and conduction into a single component and applying Newton's equation of cooling. The accumulative heat flux transported from the centroid of the solid cell to the centroid of the fluid-solid interface can be expressed as follows using Eq. 1 and Figure 4 as well as energy conservation [11]:

$$q"_{total} = \frac{\lambda_{steel}(T_{cell} - T_{face})}{\Delta y} = HTC\left(T_{face} - T_{drop}\right) + q"_R \quad (9)$$

T_{face} is the temperature of the interface centroid, T_{cell} is the temperature of the solid centroid, y is the distance between the solid and face centroids and is half the cell height, and T_{drop} is the temperature of the droplet upon impingement [11].

However, it is not feasible to evaluate the temperature of each droplet prior to and following impingement [11]. The temperature of spray water, which is observable and controllable, has been used in place of term by the steel industry since it is more practical. The current study likewise employs this criterion to provide uniform HTC values. The following expression is obtained by rearranging Eq. 9 and solving for HTC:

$$HTC = \frac{\lambda_{steel}(T_{cell} - T_{face}) - \Delta y q"_R}{\Delta y (T_{face} - T_{drop})} \quad (10)$$

2.2 Solidification of Steel

The primary goal of continuous casting (CC), as mentioned in previous sections, is to completely freeze the molten steel before the oxygen torches cut the slab into pieces, i.e., to maintain a proper metallurgical length. Because direct measurement of the metallurgical length is impractical, finding the region where the steel temperature is lower than the solidus temperature by solving the energy equation for the full steel strand is the recommended approach. As a result, and in a control system, the heat transfer solver is a critical component. The equation is simple and can be found in any heat transfer textbook. The significant challenges are boundary conditions and the computational domain's dimension.

The solidification process in CC involves a number of different physical phenomena that must be regulated in order to manage the overall product quality. Particle inclusions - primarily slag, flux

powder, or argon gas - along the solidification front, and surface defects such as oscillation marks and various surface cracks - are two of the more prominent factors contributing to decreased product quality [26-28]. While though technological progress has helped mitigate the effects of these elements during production, they continue to pose a significant risk to CC. Regulation of heat transfer and the introduction of contaminants during solidification are the two primary factors instigating these flaws, along with alterations to the material composition of the product or improvements to equipment or operating techniques upstream of the caster.

The (Mushy Zone) MZ region, which is the zone between the liquidus and solidus temperatures, is the most influential physical phenomena on flow and HT. Flow in the MZ region is slowed as hardened dendrites, which develop as a column, form along the shell front. Molten steel that moves more slowly and thickly affects both the conductive and convective HT, and therefore the shell formation. The MZ model was developed by Carman and Kozeny, and it connects the dendrites' microscopic structure to their macroscopic effects on flow and HT [29], [30].

These intricate phenomena are described in greater depth in other books [51–53]. Some of the many complicated phenomena that occur throughout the CC process are depicted vividly in Figures 2-3.

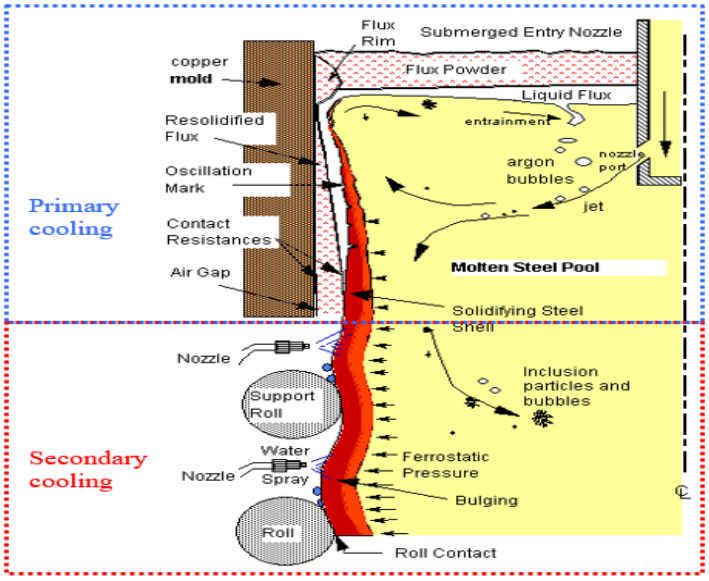

Figure 2-3: Primary and Secondary cooling physical phenomena [53]

The excess liquid is collected in the hardened steel shell, which is dragged out of the mold at high speed by rollers attached to the underside of the mold [31]. Problems with production or broken molds could result from using a steel slab that is irregular in shape and has a thin shell thickness. The major purpose of secondary cooling is to ensure slab stability in the secondary zone below the mold. Roll contact with the slab and spray nozzles are both crucial throughout the cooling process. This method of surface temperature control has the potential to dramatically eliminate defects and reheating. Some surface cracks in the slab are possible after secondary zone warming [32]. Spray cooling zones below the melt core value may allow for slab surface reheating [33]. At the mold exit, the hardened shell can grow up to 20mm-25mm on both the broad and narrow faces, as measured by the breakout shell and predicted by numerical calculations performed by Professor Brain Thomas et al. [34]. When the semi-solid slab reaches the secondary cooling portion, the spray cooling is so powerful that the liquid steel inside the solid shell continues to lose heat and solidify. As a result, during the entirety of the secondary cooling phase, the solid shell expands from the narrow face and the broad face towards its center.

Because of the high casting temperature and the mobility of the semi-liquid steel inside the solid shell, direct observation and measurement of the solidification process is nearly impossible. This is owing to the fact that the steel is moving around. In the event that breakout occurs during the process of continuous casting, there is one circumstance in which direct measurement of solid shell is not permissible. The remaining hollow solidified shell can provide great insights into the solidification process, such as the shell thickness at different locations, the oscillation mark depth and width, and inclusion entrainment. This happens once the molten steel bursts through the shell after the breakout has occurred [31].

As the shell travels between consecutive rolls in the spray zones after it has been extruded from the mold, it undergoes phase transitions and other microstructural changes that have an effect on its strength and ductility. Ferrostatic pressure, withdrawal, friction against rolls, bending and unbending, these are all variables that contribute to the thermal strain on the portion of the material. Bending and unbending also contribute. Because of the intricate stress patterns, the shell deforms and crawls as a result of the pressure. It is possible for crack growth and propagation to take place as a consequence of successive depressions in the surface of the strand [35]. Heat and solutal buoyancy effects, both of which are caused by changes in density between the various

compositions created by micro segregation, contribute to the promotion of fluid flow lower in the caster. This flow is the root source of macro segregation as well as the defects that accompany it, such as centerline porosity, cracks, and other undesired property fluctuations [36]. The steel shell is subject to a variety of deformation and fracture concerns due to creep at rising temperatures, linked metallurgical embrittlement, and thermal stress. Creep at increased temperatures.

In continuous steel casting, the production of slabs of a high quality is impossible without accurate and stringent supervision of the secondary cooling process. If the temperature profile down the caster is not calibrated to reduce stress during temperature zones of low ductility, such as unbending, failure such as transverse surface cracks may arise [37]. With thin-slab casters, where it is impossible to examine the surface for flaws and when quick casting speeds are used, cracking is made worse by the combination of a narrow machine radius and rapid casting speeds. As a result of this, there is a significant motive to use control systems in order to optimize spray cooling in order to achieve temperature profiles that are desirable.

Secondary cooling management may be challenging. Traditional feedback control systems have had difficulty using optical pyrometers due to fluctuations in emissivity caused by periodic surface scaling and the hostile environment of the steam-filled spray chamber [38] [39]. Thin-slab casting moves at a breakneck pace, requiring the operator to make split-second decisions and adjustments. With the advent of modern air-mist cooling nozzles comes the promise of faster and more uniform cooling, but also the challenge of regulating yet another process variable, that is air flow rate.There have been previous attempts made to provide real-time dynamic control of the cooling of continuous casters. The flow of the spray water should be controlled in such a way that every region of the strand's surface has the identical experience with heat. This has been recognized for a very long time. This is incredibly important both during and after transients, such as casting slowdowns that occur during ladle swaps, but it is not normally obvious to the player. sensors of temperature in a variety of forms, including optical pyrometers. Both Okuno et al. [40] and Spitzer et al. [41] proposed using real-time model-based methods to monitor the temperature in horizontal slices across the strand in order to keep the surface temperature at four to five fixed locations.

The computations were done at a pace of once every twenty seconds, and in order to calibrate the system, feedback-control sensors were utilized. These kinds of systems have been shown to be problematic in practice as a consequence of the imprecision of temperature sensors such as optical

pyrometers. Spray cooling and casting speed can both be dynamically controlled at the same time [43] according to a technique that was developed by Barozzi et al. [42]. They had little choice but to rely on feedforward control due to the slow computer speeds available at the time. This was necessary in order to get the projected temperatures to match the parameters that were chosen. Lally advised the utilization of computer models that were fundamentally based in order to maximize spray cooling in the interest of eliminating flaws [43]. Because of the slowness of the computers at the time as well as the ineffectiveness of the fundamental models and control algorithms, it was not possible to implement online control at that time.

Rolls are used to provide support for the steel so that it does not bulge as a result of the ferrostatic pressure. Diener [44] measured the temperature of the guide rollers in the secondary cooling region of a slab in a continuous caster at variety of distances from the surface of the guide rollers and without the use of any internal cooling. It was found that the rollers had a substantial impact on the cooling of the material. In order to evaluate the temperature of the slab's surface, Barber [45] utilized thermocouples that were implanted within the strand [46]. It was determined how much of a role the rollers played in the heat transmission that occurred in the secondary cooling zone.

3. METHODOLOGY

3.1 Spray Flat Fan Atomizer Model

The spray pattern and droplet size distribution of a flat fan atomizer can be simulated with the utilization of the computational fluid dynamics (CFD) model available in ANSYS Fluent. Often employed in agricultural, automotive, and industrial settings, flat fan atomizers create a fan-shaped spray pattern. The ANSYS Fluent model simulates the liquid spray using a Euler-Lagrangian method. When following the boundary between two immiscible fluids, the method is a useful numerical tool. Liquid spray and ambient air form a contact in this example. The flat-fan atomizer was used for the simulations which is extremely similar to the pressure-swirl atomizer, with the exception that it produces a flat sheet and does not employ swirl. The liquid exits from a broad, narrow aperture as a flat, droplet-forming liquid sheet. The model implies that the fan emanates from a fictitious origin. The position of this origin must be provided, which is the junction of the lines denoting the fan's sides and the center point of the arc from which the fan starts. ANSYS FLUENT will identify the direction of the injection by locating the vector that extends from the origin to the center point. Also, the half-angle of the fan arc, the width of the orifice (in the normal direction) and the mass flow rate of the liquid to utilize the flat-fan atomizer model, must be provided.

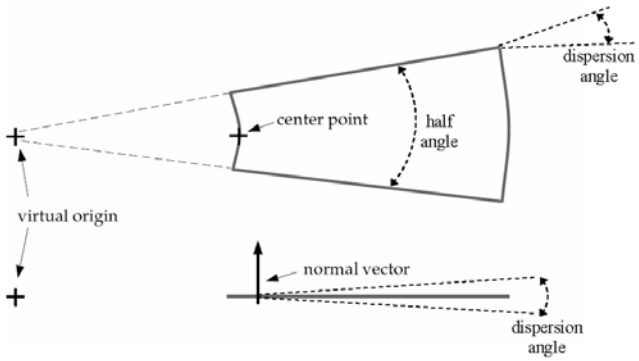

Figure 3-1: Positioning and angles

3.1.1 Model development

Spray cooling is used to ensure that the steel can cool and solidify at the rate required to achieve the required production rate. The process uses a set of nozzles to spray water onto the surface of the solidifying steel. The quality of the ultimate product is directly related to uniform cooling, and because of that, it is one of the crucial elements within the body of steel production, ensuring a uniform cooling allows for the avoidance of breakout and bulging of steel as it is being solidified throughout the cooling process. Therefore, the study of overlap in spray cooling is essential for achieving uniform cooling and accordingly, producing high-quality steel. Spray cooling results in heat extraction, which gives rise to the heat extraction coefficient. It is crucial to obtain the maximum and uniform of heat transfer coefficient to allow for maximum steel cooling. HTC can be estimated using several correlations, some of which are extensively utilized by researchers. In the 1970s, Nozaki and his team accomplished significant empirical correlations for the HTC and high-temperature surfaces [48]. Nozaki developed the HTC correlation below which has been widely adopted by numerous researchers.

$$HTC = f(\dot{W}, Tw, \alpha) = 1570\,\dot{W}\frac{0.55(1 - 0.0075\,Tw)}{\alpha} \quad (11)$$

Equation (19) provides a correlation between the HTC and the water spray density distribution, W, and water temperature, Tw. The primary issue is that the parameter involved in the correlation is caster-dependent and cannot be precisely determined.

Therefore, the parameter might be considered a fitting parameter. Zhang [5] modified Nozaki's correlation, selected a specific value for the parameter, and reported the correlation for the HTC as follows:

$$HTC = f(\dot{W}, Tw) = 5849\,\dot{W}\,0.451(1 - 0.0075Tw) \quad (12)$$

For estimating the HTC for water-spray cooling nozzles, these correlations exhibit a variety of relationships of varying complexity and taking into account a number of parameters. To create high-quality and high-strength steel, the spray cooling rate in the secondary cooling region must be properly developed and managed. Alternatively, and based on (Laitinen and Neittaanmaki, 1988; Sengupta et al., 2005), an unevenly distributed temperature field within the solidified shell on the slab can create lingering thermal strains and tensions that cause cracking and other defects. It is impossible to measure the temperature distribution during continuous casting within the

solidified steel. It was also advised to test the uniformity and strength of spray cooling using HTC on the steel surface. Newton's law of cooling is used to obtain HTC, which is used to describe heat transfer [10]:

$$q''total = \_q''cond + q''conv + qR'' = HTC\_(Tface - Tspray) + qR'' \quad (13)$$

As shown in above equation, HTC is the result of conduction, which occurs when a water droplet touches a hot steel surface, and convection, which results from air entrainment. Equation 21 highlights the essence of casting control systems utilized in contemporary steel mills. This simulation was modelled and simulated in Fluent. The study investigates the cooling of a steel slab by 2 adjacent nozzles with overlap. In a continuous caster, it is common practice to position two adjacent nozzles with a small spray overlap to achieve uniform cooling. Hence, one of the key factors that affects the effectiveness of spray cooling in continuous casting is the overlap between adjacent nozzles. If the overlap is too large, it may result in higher heat extraction within the overlap region. On the other hand, if the overlap is too small, it may result in lower heat extraction within the overlap region. Both scenarios will render with non-uniform cooling, accordingly a uniformity in cooling is the desired outcome of this study. Consequently, the objective of this research is to optimize the overlap in spray cooling while considering various factors, including the behavior of the coolant, the temperature of the metal, and how such factors interact holistically with the presence of overlap. Researchers have explored various techniques to optimize the overlap in spray cooling, including computational fluid dynamics (CFD) modeling, experimental studies, and statistical optimization methods. This study will focus on the CFD approach and discuss the findings.

3.1.2 Governing equations

Continuous phase (air)

The following equations characterize the air phase's motion in a Eulerian reference frame.

Continuity equation:

$$\frac{\partial \rho_{air}}{\partial t} + \nabla.(\rho_{air} u_{air}) = 0 \quad (14)$$

where ρ_{air} is the air density, and u_{air} is the air velocity

Momentum equation:

$$\frac{\partial}{\partial t}(\rho_{air} u_{air}) + \nabla.(\rho_{air} u_{air}^2) = -\nabla P + \nabla(\mu_{air} \nabla. u_{air}) + \rho_{air} g + S_{air-drop} \quad (15)$$

where $S_{air\text{-}drop}$ is the source-term coupling the momentum of the air with that of the droplets according to the following expression:

$$S_i = \frac{\pi}{6\rho v_{cell}} \sum \dot{\eta} \left(\rho_{drop}^{out} u_i^{out} \left(d_{drop}^{out} \right)^3 \right) - \rho_{drop}^{in} u_i^{in} \left(d_{drop}^{in} \right)^3 \quad (16)$$

The momentum between the air and the drops in a certain cell of the fixed grid is equal to the change in momentum of all the drops (g) passing through it, throughout the time-step, according to the particle source in cell model [48].

Most of impinging jets used in industrial applications generate turbulent flow due to the formation of vortices along the jet's surfaces, that is similar to the Kelvin-Helmholtz instability. Predicting the presence of turbulence with precision is very difficult and barely feasible. According to the exhaustive comparisons made by [49], the Shear Stress Transport (SST) model by Menter [50] is one of the most accurate and computationally efficient turbulence models for forecasting impinging jet flow. The SST model combines the k–ω and the k–e models, the former near the wall, which requires a finely spaced mesh close to the wall to generate accurate results, and the latter farther from the wall to increase the accuracy of the results by capitalizing on the strengths of each model.

Atomization

According to the atomizer's operating flow parameters, the liquid jet can experience a variety of instability problems, including capillary, helical, and Kelvin-Helmholtz (KH) instability. Previous studies have also identified a number of processes that lead to ligament and liquid core disintegration. To establish the primary disintegration length for air-blast nozzles, several researchers carried out experimental experiments and proposed empirical correlations. Within the spray stream, the velocity and size distributions of the droplets which are frequently used to illustrate this, are determined by the hydrodynamics inside the atomizer and the breakdown of the liquid sheet. Primary breakup, refers to the first breakup processes that occur when droplet-droplet collisions or aerodynamic instabilities lead the primary breakup droplets to further split apart into smaller droplets (see Figure 1).

According to the atomizer's operating flow parameters, the liquid jet can experience a variety of instability problems, including capillary, helical, and Kelvin-Helmholtz (KH) instability. Previous studies have also identified a number of processes that lead to ligament and liquid core disintegration. To establish the primary disintegration length for air-blast nozzles, several researchers carried out experimental experiments and proposed empirical correlations [40,41,45-47]. The separation length was estimated to be [40] in this study.

$$\frac{L}{D_l} = 0.66 We_g^{-0.4} Re_l^{0.6} \tag{17}$$

Droplet coalescence and breakup

The O'Rourke approach serves as the basis for the droplet coalescence model [53], which has estimation of stochastic collisions. The relative velocity of the droplet with regard to the surrounding air causes droplet fragmentation, which is taken into consideration by the WAVE breakdown model. The Kelvin-Helmholtz instability with the fastest growth rate is assumed to be the basis for the model's estimation of the breakup time and size of the subsequent offspring droplets:

$$\frac{dr_{parent}}{dt} = \frac{\Lambda\Omega(r_{parent} - r_{child})}{3.726 B_1 r_{parent}} \tag{18}$$

Droplet motion and convective heat transfer

The approach used to model the motion of the droplets is Langrangian. The following is how their Newton-based motion equation accounted for both aerodynamic drag and gravitational force:

$$\frac{du_{drop}}{dt} = \frac{3\mu_{drop} C_D Re_{drop}}{4\rho_{drop} d_{drop}^2}\left(u_{air} - u_{drop}\right) + \frac{g(\rho_{drop} - \rho_{air})}{\rho_{drop}} \tag{19}$$

The coefficient of drag, CD, which measures the air-droplet interaction, can be estimated utilizing the piecewise function in [57]. Due to being on the order of the gas-to-droplet density ratio, other aerodynamic forces that may have an impact on droplet motion were disregarded [59], and in this case it is 10^-3. The Saffman lift and Magnus forces were also disregarded because the drops are not in a high-shear area of the flow field across most of the field [59] which was acceptable as this paper did not explore the drops motion near the plane of impact. Individual droplet trajectories are calculated periodically throughout the continuous phase's iterations. On the basis of the change in

the position vector components of the droplets over time, the following formula was used to calculate their trajectory:

$$\frac{dx_{drop}}{dt} = u_{drop} \tag{20}$$

The drag force term, which is included in the momentum equation of air as a source, is used to simulate the interaction between air and droplets.

The following droplet energy balance equation is used to calculate droplet temperature variations throughout the spray cooling process:

$$m_{drop} c_p \frac{dT_{drop}}{dt} = \pi d_{drop}^2 h\left(T_\infty - T_{drop}\right) + \frac{dm_{drop}}{dt} h_{fg} + \pi d_{drop}^2 \varepsilon_{drop} \sigma_{SB}\left(T_R^4 - T_{drop}^4\right) \tag{21}$$

The Ranz-Marshall model can be used to compute h, the convective heat transfer coefficient [155]. The rate of droplet vaporization is determined by the concentration difference between the droplet surface and the airstream, and the formula below can be used to determine the droplet's associated mass change rate.

$$\frac{dm_{drop}}{dt} = \pi d_{drop}^2 k_c (C_s - C_\infty) \tag{22}$$

The coefficient kc in Eq. (6) can be obtained from the Sherwood number correlation with the similar form as Eq. (8):

$$Sh_{drop} = \frac{k_c d_{drop}}{D_{vapour}} = 2.0 + 0.6 Re_{drop}^{0.5} Sc^{0.33} \tag{23}$$

Droplet-wall impingement model

The stick, reflect, and wall jet outcomes are all considered in the wall jet model that was established by Naber and Reitz [58] based on the characteristics of each droplet. After impingement, the droplet in the stick mode stays in touch with the wall and keeps evaporating. In reflect mode, a particle's normal velocity component takes on the opposite sign but the tangential and normal velocity components' magnitudes stay the same. In the wall jet mode, the model simulates an inviscid liquid jet that is released from the stagnation point and impacts a solid surface with a continuous stream of closely spaced droplets. In the analytical solution for an axisymmetric impingement, the empirical function for the liquid jet with a height of H as a function of the angle at which the droplet departs the horizontal impingement is utilized:

$$H(\Psi) = H_\pi e^{\beta\left(1-\frac{\Psi}{\pi}\right)} \tag{24}$$

The probability that a droplet leaves the impingement point at an angle between Ψ and $\Psi + \Delta\Psi$ is given by integrating the expression for (Ψ):

$$\Psi = -\frac{\pi}{\beta}\ln\left[1 - P\left(1 - e^{-\beta}\right)\right] \tag{25}$$

The expression for β is given as:

$$\sin(\emptyset) = \frac{e^{\beta-1}}{(e^{\beta}-1)\left(1+\left(\frac{\pi}{\beta}\right)^{2}\right)} \tag{26}$$

Impingement heat transfer model

Even though a droplet is expected to maintain its spherical shape throughout its lifetime, it may deform and remain in close contact with the solid surface following an impact. The quantity of heat exchanged between the droplet and the solid container can be calculated using pure heat conduction as follows:

$$\frac{d}{dt}\left(m_{drop}c_p T_{drop}\right) = \frac{k_{drop}A_{cond}}{s_{slab}}\left(T_{slab} - T_{drop}\right) \tag{27}$$

The effective contact area A_{cond} between droplets and walls is determined using the expression in [60]. The Leidenfrost temperature is lower than the slab temperature during the casting process [61]. predicting vaporization from discrete phase droplets using droplet vaporization. It starts when the temperature of the droplet exceeds the vaporization temperature and continues until the temperature of the droplet reaches the boiling point or the volatile component of the droplet is completely consumed. Given the slab's high temperature, it is anticipated that the vaporization rates will be considerable, and as a result, the influence of the evaporating material's convective flow from the droplet surface to the bulk gas phase will be significant. The droplet vaporization was modeled using the convective/diffusion-controlled model of [62].

Slab movement

The impact of the slab's movement with respect to the orifice was simulated in the simulations using both the moving reference frame and the stationary reference frame. While the energy equation for a moving substrate in the computational domain is defined as follows, the governing equations for air and droplets are solved with reference to a stationary reference frame:

$$\frac{\partial}{\partial t}\left(\rho_{steel}h_{steel}+\frac{\overline{|u|}_r^2\rho_{steel}}{2}\right)+\nabla.\left[\bar{u}_r\left(\rho_{steel}h_{steel}+\frac{\bar{u}_r^2\rho_{steel}}{2}\right)\right]=\nabla.\left[k_{steel}\nabla T+\bar{\bar{\tau}}\bar{u}_r\right] \quad (28)$$

Relative velocity, $\bar{u}_r$ between the two reference frames is defined as:

$$\bar{u}_r=\bar{u}_{stationary}-\bar{u}_{moving} \quad (29)$$

Prior to impingement, 50 continuous phase iterations were made between two discrete phase iterations; after droplet impingement on the slab surface, 500 continuous phase iterations were made between two discrete phase iterations. Particle radiation interaction, two-way coupling, stochastic collision, coalescence, and breakdown models were used to simulate the discrete phase. ANSYS Fluent 2020R1 was the program used to execute all the cases, and it took 48 processors about 3 hours to converge each example.

3.2 Solidification model

3.2.1 Simulation approach

In this study, the Eulerian Volume-Of-Fraction model is used to simulate the phase change and convection within the semi-solid steel slab. Steel in liquid form and steel in solid form are handled as two immiscible continuous phases. One set of conservation equations governs the fluid flow in the regions of molten steel, mushy zone, and solid. Conductive to estimating turbulence in the flow model, the Reynold Average Navier-Stokes (RANS) k-shear stress transport (k- SST) model is utilized. This model combines the most advantageous characteristics of the standard k-model and the k-model. The k- SST utilizes blending functions to manage obstacles such as walls and baffles more effectively than the classic k- model, and it also anticipates flows with separation and unfavorable pressure gradients more accurately than the k- model [47].

A modification to the solidification model was achieved through taking into account the curvature of the caster while also considering the computational expenses of the simulation casefile. The goal of the aforementioned modification is to predict and visualize the metallurgical length in one simulation rather than nine. Moreover, previously in each segment, the top surface is assigned the velocity profile from the downstream of its preceding segment, which leaves a room for human errors as there would be a decent amount of input and output files that may hinder the quality of the results. Also, not neglecting the curvature of the slab can result in a more realistic approach to the prediction of the metallurgical length. Figures 3-2 and 3-3 illustrate the slab caster used in the simulation.

Using Star-CCM+, a curved model of the caster was designed. Foreseeing the behavior of steel as it travels from the mold section and down to the secondary cooling section. The current geometry is designed for the means of predicting metallurgical length. Hence, and for computational expenses as well, the portion of the caster where steel is liquid and transitioning to its solid state and up to the first point of complete solid steel is only modelled.

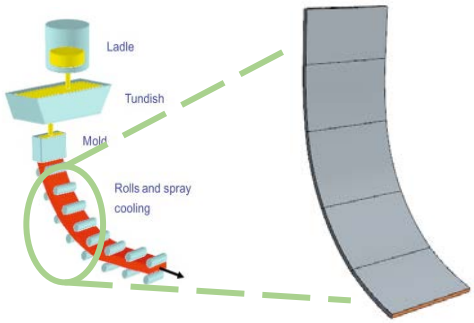

Figure 3-2: Geometry Design of the Curved Caster

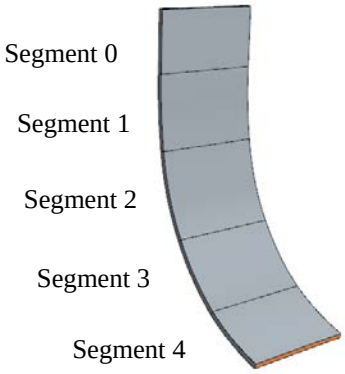

Figure 3-3: Solidification simulation

3.2.2 Governing equations

Mass conservation

The following is an example of how the equation for the conservation of mass in an incompressible and isotropic Newtonian fluid could be written:

$$\frac{\partial \rho_{\text{steel}}}{\partial t} + \nabla \cdot (\rho_{\text{steel}} \vec{u}_{\text{steel}}) = 0 \tag{30}$$

Where ρ_{steel} and $\vec{u}_{steel}$ are the density and velocity of the liquid and solid mixture, respectively.

Momentum conservation

At varying temperatures, steel alloys undergo the solidification process. The temperatures at which a substance can be considered solid or liquid correspondingly establish the lower and upper bounds of the temperature range. One equation for the conservation of momentum is solved across the entirety of the computing domain.

$$\frac{\partial}{\partial t}(\rho_{\text{steel}} \vec{u}_{\text{steel}}) + \nabla \cdot (\rho_{\text{steel}} \vec{u}_{\text{steel}}) = -\nabla P + \nabla\left[\mu_{\text{eff}}(\nabla \vec{u}_{\text{steel}} + \nabla \vec{u}_{\text{steel}}^{T})\right] + \rho_{\text{steel}} \vec{g} + S_{\text{porous}} \tag{31}$$

Where P is pressure, μeff is effective viscosity, and it alters the viscosity of the liquid in the zone of free-floating dendrites, S_{porous} is a momentum source term that has an influence in the porous region.

Turbulence model

Because of its precision and ease of computing, the k- SST model has been selected as the one to use for turbulence modeling. The formula for this model is as follows:

$$\frac{\partial}{\partial t}(\rho_{\text{steel}} k) + \nabla \cdot (\rho_{\text{steel}} k \vec{u}_{\text{steel}}) = \nabla \cdot \left[\left(\mu_{\text{eff}} + \frac{\mu_t}{\sigma_k}\right) \nabla k\right] + G_k - \rho_{\text{steel}} \beta_k k\omega + S_k \tag{32}$$

$$\frac{\partial}{\partial t}(\rho_{\text{steel}} \omega) + \nabla \cdot (\rho_{\text{steel}} \omega \vec{u}_{\text{steel}}) = \nabla \cdot \left[\left(\mu_{\text{eff}} + \frac{\mu_t}{\sigma_\omega}\right) \nabla k\right] + G_\omega - \rho_{\text{steel}} \beta_\omega \omega^2 + S_\omega \tag{33}$$

Where k represents the turbulence kinetic energy, ω represents the turbulence dissipation rate, μ_t is the turbulent viscosity, G_k represents the creation of turbulence kinetic energy due to mean velocity gradients, σ_k and σ_ω are the turbulent Prandtl numbers, ω is the generation of turbulence dissipation rate. β_k and β_ω are model coefficients while S_k and S_ω are source terms that are used to account for the mushy zone's existence.

Energy conservation

The Enthalpy-Porosity model that was utilized for this research does not follow the liquid-solid interface in an explicit fashion. To calculate the solid distribution, the model makes use of an enthalpy formulation, which results in a noticeable attenuation in the amount of required time for computation. The law of the energy conservation can be expressed as follows for both liquid and solid states:

$$\frac{\partial}{\partial t}\left(f_{liq}\rho_{liq}h_{liq}\right) + \nabla\cdot\left(f_{liq}\rho_{liq}h_{liq}\vec{u}_{liq}\right) = \nabla\cdot\left(k_{liq}\nabla T_{liq}\right) - S_{liq-sol} \quad (34)$$

$$\frac{\partial}{\partial t}\left(f_{sol}\rho_{sol}h_{sol}\right) + \nabla\cdot\left(f_{sol}\rho_{sol}h_{sol}\vec{u}_{sol}\right) = \nabla\cdot\left(k_{sol}\nabla T_{sol}\right) - S_{liq-sol} \quad (35)$$

In this context, the subscripts liq and sol indicate that we are talking about liquid and solid, respectively. The symbol for density is ρ, the symbol for sensible enthalpy is h, the symbol for velocity $\vec{u}$, the symbol for thermal conductivity is k, the local temperature is T, the energy exchange between liquid and solid is $liq{-}sol$. Each control volume's liquid and solid fractions have to demonstrate that they can adhere to the following constraint:

$$f_{liq} + f_{sol} = 1 \quad (36)$$

The liquid enthalpy shown in Eq. (185) is calculated by:

$$h_{liq} = h_{sol} + h_{lat} \quad (37)$$

4. BOUNDARY CONDITIONS AND COMPUTATIONAL DOMAIN

4.1 Flat fan atomizer model

4.1.1 Nozzles comparison and methodology

When it came to modeling the spraying system, two different models were used as an approach. Two distinct models: one is air mist spray and another is hydraulic nozzle. Flat fan atomizer model in Fluent is one type of hydraulic nozzles. Both air mist spray and hydraulic nozzle methods are important to discuss because each was developed for a distinct objective, and both are regarded as being equally necessary for the completion of this project. When using such a technique, the air mist spray simulation provides higher resolution quality of results "per spray," but it is computationally expensive to do so, particularly if multiple spray scenarios are required as it has a 4 steps approach. On the other hand, the flat fan atomizer model produces a quality that is above average but not quite as high as the quality produced by the first method. In spite of this, it has a low computational cost and can be of great assistance in situations where multiple simulation scenarios and a parallel method for running multiple scenarios of spraying simulations are required. For the purpose of this thesis, we will be utilizing the latter method, as the "mapping" approach that will be implemented for the spraying system as a whole has been designated as the project's current top priority. Figure 4-1 illustrates a comparison between the two aforementioned models.

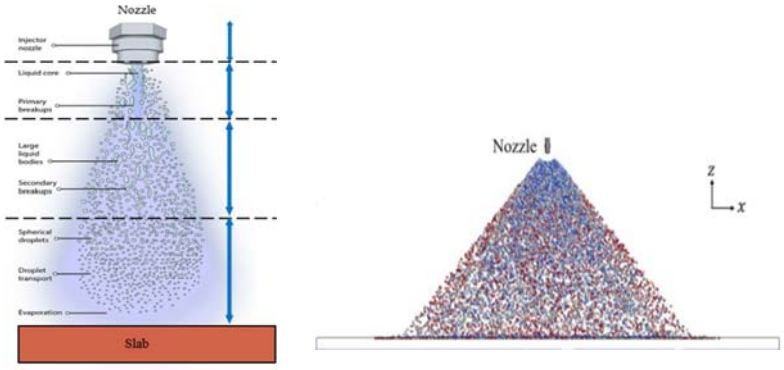

Figure 4-1: Air mist spray (4 steps) and flat fan atomizer models

The casting parameters that were simulated can be found in Table 4-1 below. These parameters were used to carry out a study on the effects of casting speed, water flow rate, spray angle and stand-off distance, as well as to produce an HTC interrelation using these parameters. A non-slip condition was imposed on the nozzle walls, and the water inlet was modeled as a mass flow inlet. In every one of the conditions that were simulated, the temperature of the water at the inlet was kept at 300K.

Table 4-1. Casting parameters

Water flow rate (ml/s)	126.18, 233.4
Casting speed (m/min)	1.016
Standoff distance (m)	0.13, 0.15, 0.17, 0.216
Spray angle (degrees)	90, 115, 120

As mentioned before, and to develop an HTC interrelation using these parameters, the outcome of this point will then be the boundary condition to the solidification model. Furthermore, a change of the mapping method used will be discussed as the curvature of the caster imposes a curving of the flat map to a curved one.

4.1.2 Computational domain and mesh

As it can be seen in Figure 4-2, the geometry consists of a flat, solid, steel foundation with an air zone superimposed on it. The coverage area of the sprays and the height of the sprays from the steel slab are what determine the length and height of the domain, respectively. The length of the computational domain is 1300 millimeters, the width is 500 millimeters, and the height is 320 millimeters. The field can be broken down into two distinct categories: fluid and solid. The spray nozzle and the air around it make up the fluid component, while the steel slab is the indicator for the solid component.

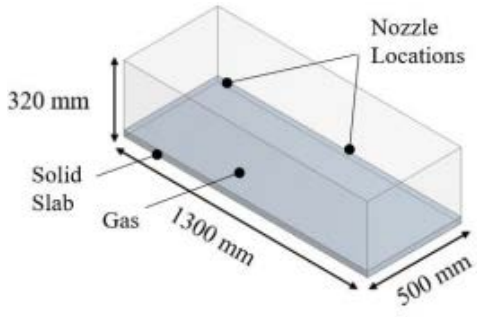

Figure 4-2: Computational Domain

Figure 4-3 demonstrates a structured mesh that represents the domain. This mesh has a total of 929556 nodes with an element size of 29.3 millimeters. Because the slab's top surface is the major surface of interest, fine mesh is utilized in the area close to that surface. It is necessary to size the edges of the mesh in order to achieve linearity. For the fluid surface, sizing of 150 is applied, however for the steel slab edge, sizing of 30 divisions in 4 conjunctions with a bias factor of 10 is utilized.

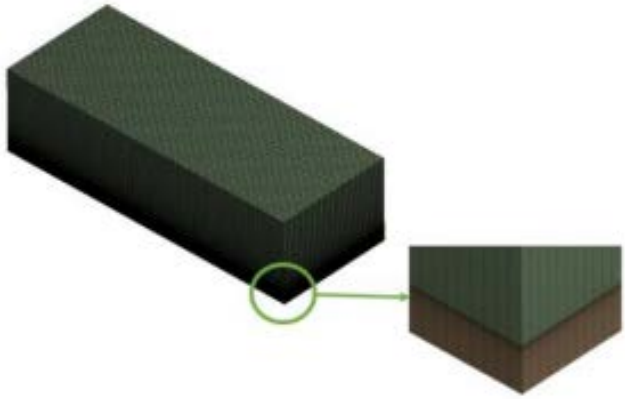

Figure 4-3: Mesh Domain

4.1.3 Impingement and mapping

A conceptual investigation of the impingement of sprays on the slab surface was carried out for a variety of varied and multiple spray parameters. Earlier than the assembly of the required distribution along the caster, some calculations were carried out. In order to have a better knowledge of the coverage area for each spray scenario that was required, the calculations included several variations in the parameters that were used for spraying, and then they assembled

everything into one large profile. For instance, figure 4-4 shows and example of the conceptual study carried out for the stand-off distance (SD).

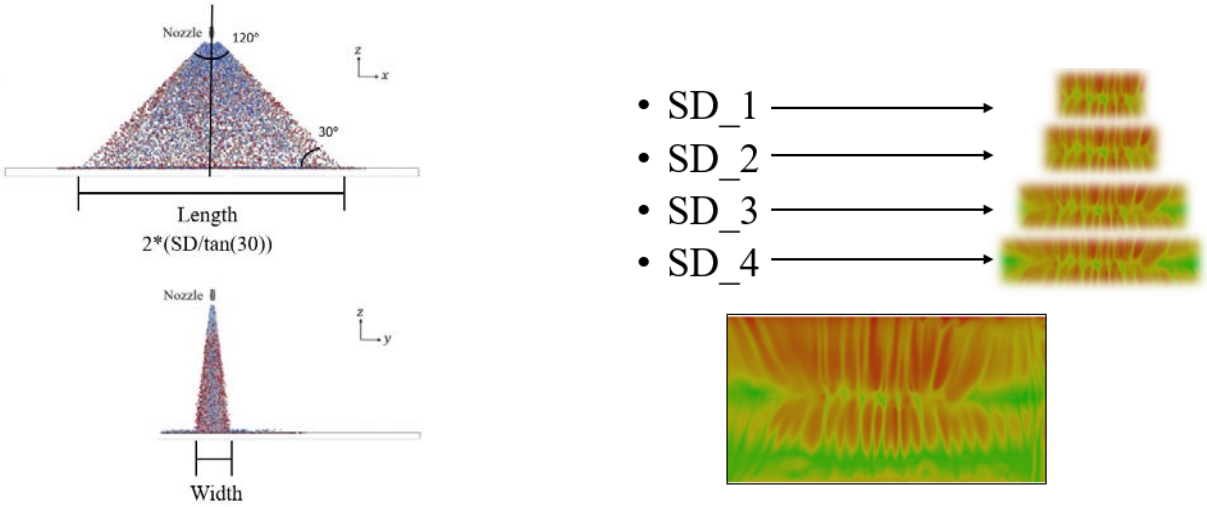

Figure 4-4: Standoff distance coverage area calculations (Left) and Coverage area imprints due to various stand-off distances (Right)

The next step would be to take the "flat" profile created and bend it to associate with the curvature of the caster. All of which will be discussed in the next solidification model section.

4.2 Solidification model

Previously, and because it was determined that the length of the caster was excessively long, to the point where it would be computationally expensive to run simulations with the full length, the caster was divided into its segments, and the simulation was carried out by moving from one segment to the next segment in order to complete the task. At the beginning of each segment, the top surface is given the velocity profile that was measured downstream in the segment that came before it. In the downstream, the boundary condition is determined by the presence or absence of a pressure outlet.

For the current approach, the modified solidification model was done to include the curvature of the caster strand as shown in Figure 4-5. This is an improvement from the simulations in the previous year where each segment was simulated individually as a flat segment. The goal of the aforementioned modification is to predict and visualize the metallurgical length in a curved strand

in one simulation rather than multiple flat segments. Moreover, and due to the fact that previously in each segment, the top surface is assigned the velocity profile from the downstream of its preceding segment, a room for human errors is left as there would be a decent amount of input and output files that may hinder the quality of the results. Also, not neglecting the curvature of the slab can result in a more realistic approach to the prediction of the metallurgical length.

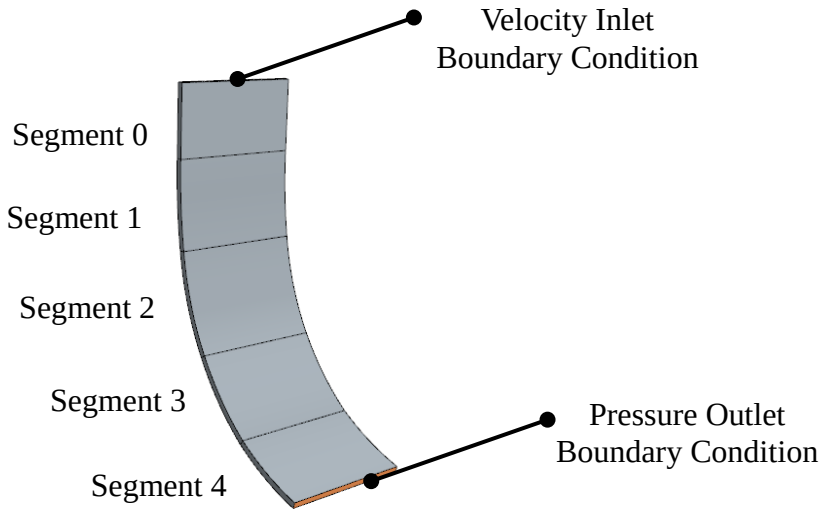

Figure 4-5: Solidification simulation model

4.3 Integration model

4.3.1 A holistic mapping of the spray profiles

The spray profiles were replicated and had placement modifications in the integration model. Based on specifications provided, the spray patterns seem to be classified based on arrangement and overlap occurrence. For instance, sprays existing in Segment 0 right after the mold seems to have the same standoff distances and a uniform distribution that has a specific percentage of overlap. On the other hand, Spray arrangement differs when moving to segments 1-6 as the standoff distances start to be varying from one location to another and overlap occurrence becomes less probable. Figure 4-6 illustrates the mapping of spray HTC onto the broad face of a segments.

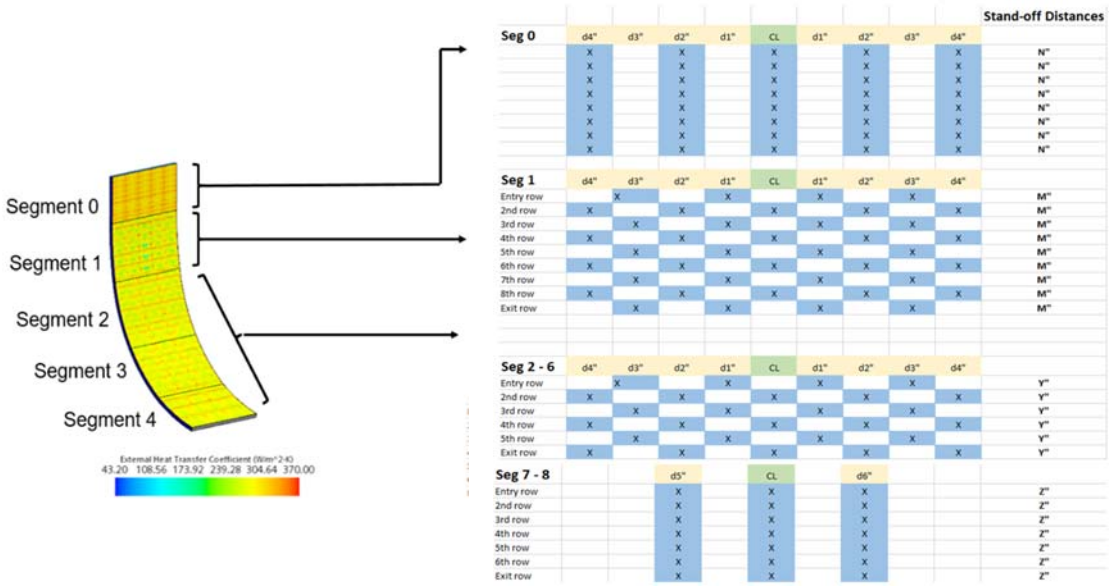

Figure 4-6: Spray HTC mapping unto the BF

Utilizing a couple of Matlab codes, two approaches were used to map the HTC profiles, depending on the spray patterns shown in Figure 4-6. One code was used to cut and replicate the area of overlap from one profile and then assembled again to form a row and then replicate that row along the specified segment, Figure 4-8 illustrates the mechanism used for such assembly. Also, for the rest of the patterns that coexist with the previously mentioned one but along other segments, another algorithm was used to proceed with the spread of HTC profiles as illustrated in Figure 4-9.

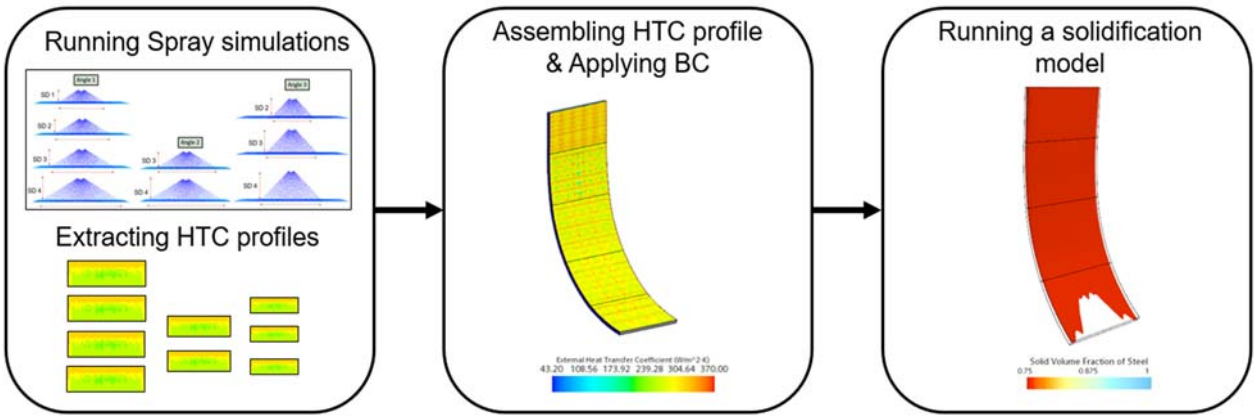

Figure 4-7: Integration methodology

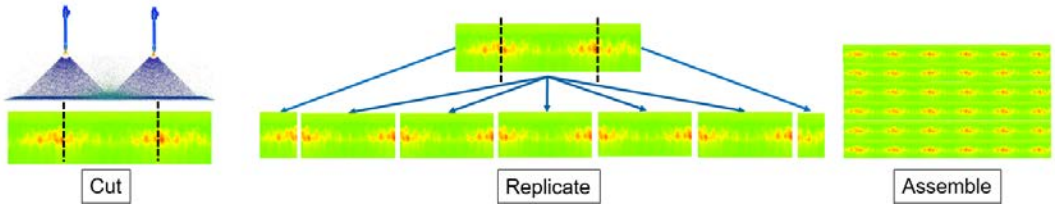

Figure 4-8: Boundary conditions for Segment 0 of the slab

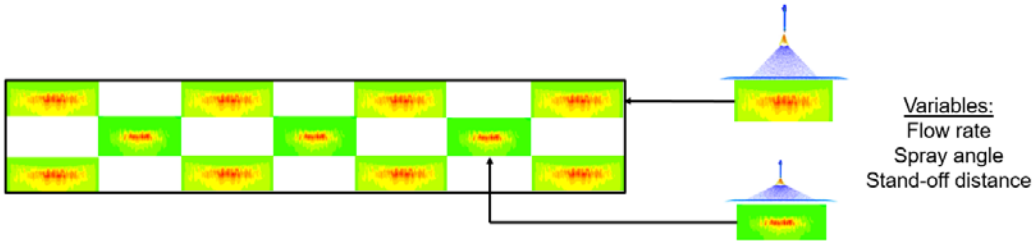

Figure 4-9: Boundary conditions for Segments 1-6 of the slab

4.3.2 Applying the Boundary condition into a curved caster

A horizontal projection was created utilizing MATLAB, where the code converts the flat HTC mapping done previously into a curved one. Such conversion was done by extracting coordinates from the geometry in Star CCM+, storing it into arrays and then using a mathematical interpolation to convert the coordinates of the HTC values to be projected into a curved plane such that a better and more accurate spread of values is achieved. Figure 4-10 illustrates the methodology behind the mentioned approach. Additionally, a geometrical domain extension for further studies was included.

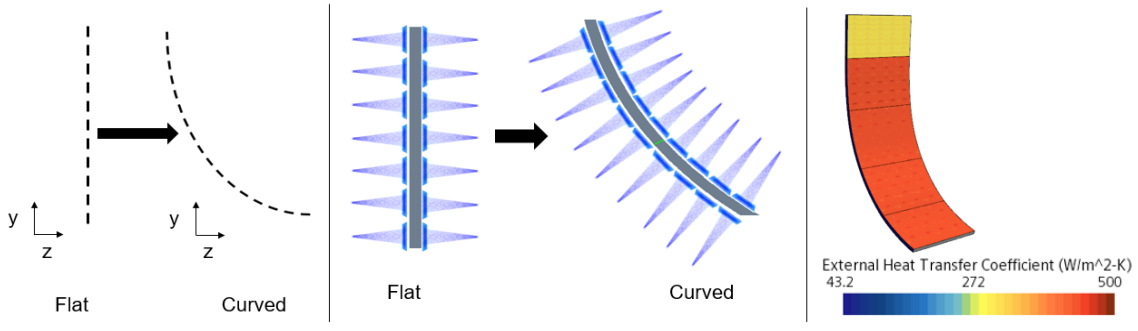

Figure 4-10: Coordinated conversion methodology

5. RESULTS AND DISCUSSION

5.1 Flat fan atomizer model

ANSYS Fluent's flat fan atomizer model is a spray modeling technique used to simulate the spray behavior of a flat fan atomizer. Typical applications for this model include agricultural spraying, industrial coatings, and combustion processes. The flat fan atomizer model is based on the Eulerian-Lagrangian method, which includes solving the governing equations for the continuous phase (i.e., the gas or liquid) with the Eulerian method and tracking the dispersed phase (i.e., the spray droplets) with the Lagrangian method.

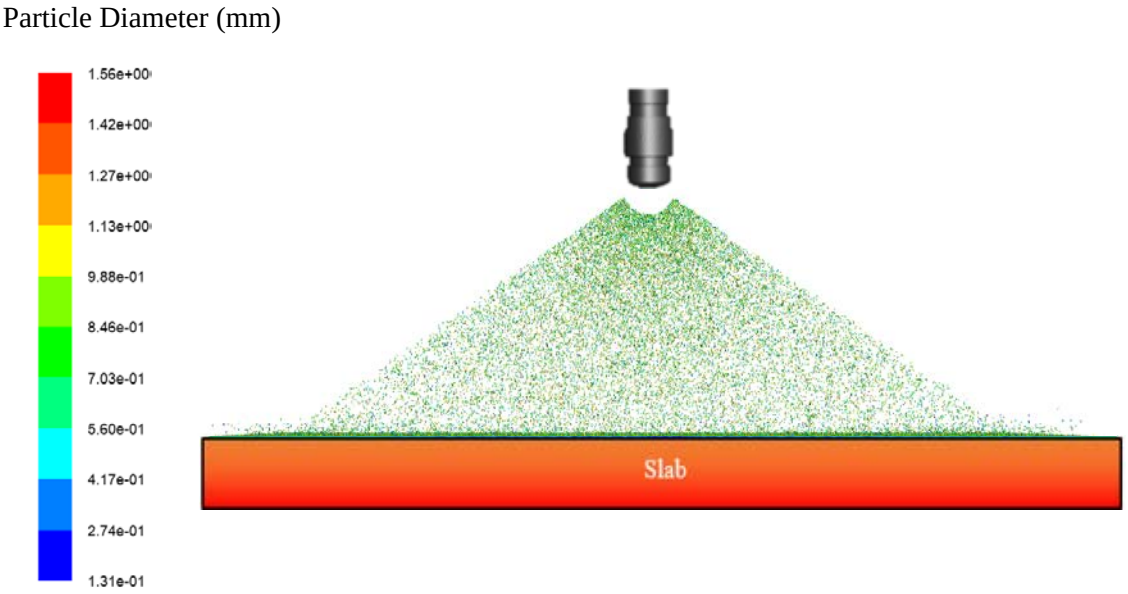

Figure 5-1: Flat fan atomizer

Using the flat fan atomizer model in ANSYS Fluent provides the following benefits:

- It can accurately predict the spray droplet size distribution, which is essential for optimizing spray performance and minimizing waste.
- It employs efficient numerical algorithms and parallel processing techniques to solve the governing equations, allowing simulation of complex spray geometries and large-scale spray systems.
- It can simulate a variety of spray systems, including those with multiple injectors, non-uniform inflow conditions, and intricate geometries.

5.1.1 Spray simulations & their combination

A flat fan atomizer model was used to model the impingement of sprays under different conditions on a slab surface. After analyzing the data provided, the scenarios of which the spray simulations were existing within the caster were cut down to 9 spray conditions, in addition to that of the overlap. Hence, after running the simulations required and classifying them based on conditions like standoff distance, water flow rate and spray angle, Matlab was utilized to solve the problem of spreading the profiles along the caster efficiently. Figure 6 shows a simple illustration of the 9 spray conditions.

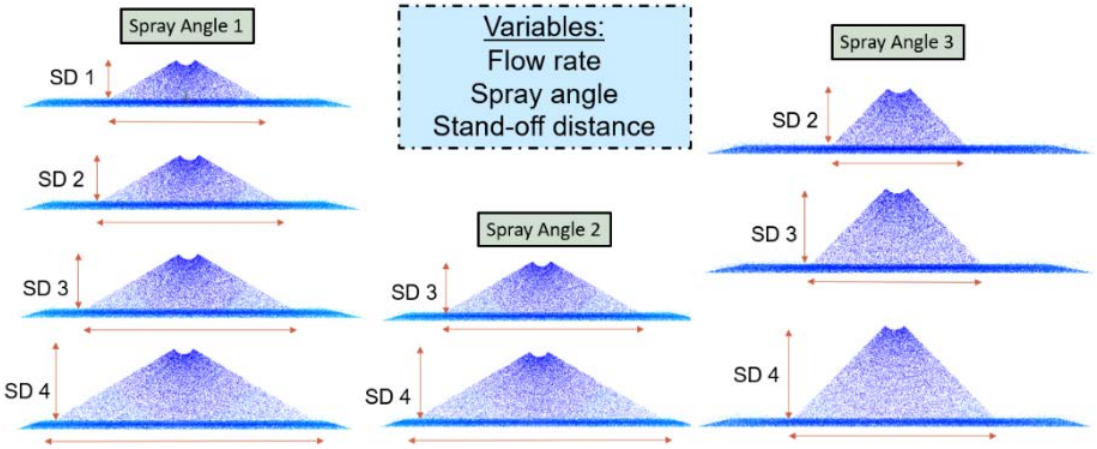

Figure 5-2: Spray conditions utilized for the spray system arrangement.

5.1.2 Spray Overlap (Parametric Study)

Furthermore, a study on the uniformity of cooling while having an overlapping sprays scenario was conducted. Optimum overlap is needed to achieve uniform cooling which can help with preventing breakout and bulging. Therefore, three scenarios were conducted to study the effect of overlap and find the most uniform cooling among them.

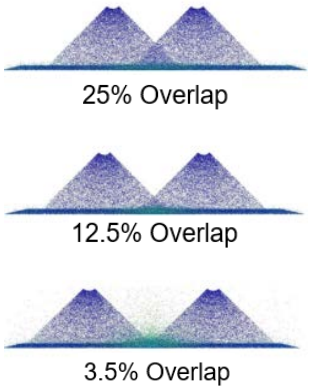

Figure 5-3: Overlap scenario

Using the flat fan atomizer model mentioned previously, different combinations of overlap nozzles were tested out. The heat transfer coefficient was observed and an optimum overlap was found. The overlap was calculated through the nozzle to nozzle distance (D) between the two air-water spray and the spray angle. They were tested on the nozzle parameters identical as used in above cases. Following is the case associated with 3.5% of overlap between 2 nozzle air-water spray (Baseline Case).

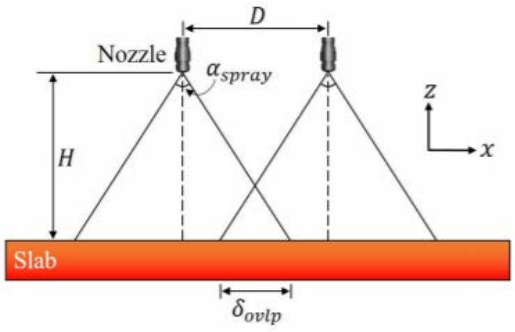

Figure 5-4 (a): Nozzle to Nozzle distance (D) and Stand-off distance (H) [54]

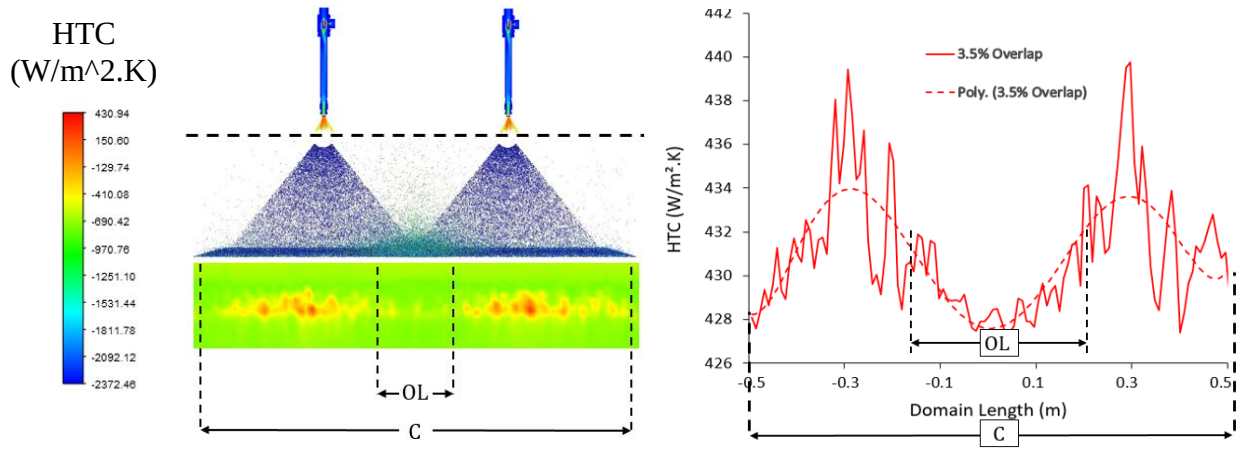

Figure 5-4 (b): Overlap HTC analysis and distribution along domain

It was concluded through the results that with less amount of overlap, there is no significant change in the cooling. The main heat extraction is taking place in the central regions of individual nozzle. So, a 3.5% overlap did not show significant effect of heat extraction which lead to undercooling in the overlap region, the 25% case showed an overcooling problem and last but not least, the 12.5% of overlap showed the most uniform distribution of heat extraction, resulting in being the optimum overlap percentage.

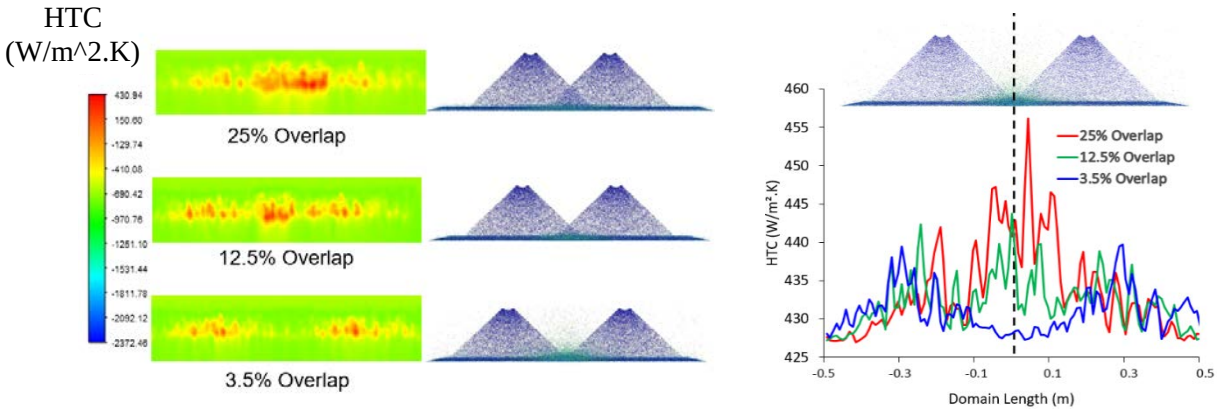

Figure 5-5: Overlap HTC analysis for three scenarios

6th order polynomial trend lines used for a good representation of over cooling, undercooling and uniform cooling and it can be confirmed again that HTC distribution within the 12.5% of overlap showed the best uniformity.

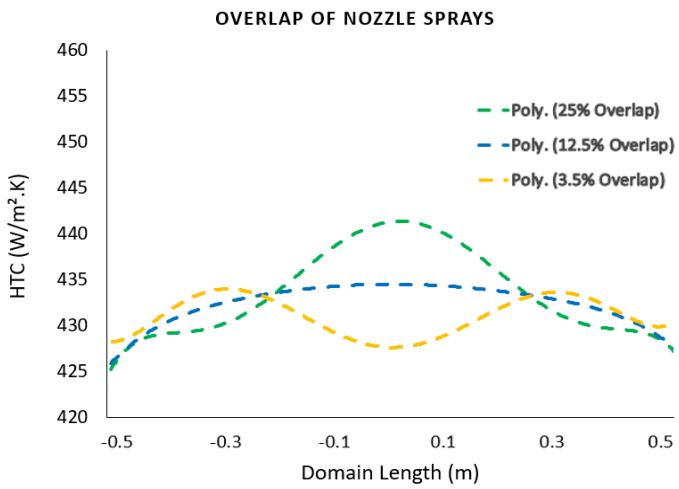

Figure 5-6: Polynomial average of the simulations

Further studies were conducted for the effect of standoff distance, therefore making the overlap analysis approached from two points of view. Furthermore, an analysis of multiple phenomena was also conducted such as moisture concentration, droplet concentration and average droplet diameter.

5.2 Solidification model

As can be depicted in Figure 5-7, the solidification model has been updated to account for the caster strand's curvature. When compared to previous work by Haibo Ma and Vitalis Anisiuba [54] [55], in which each segment was simulated separately as a flat segment, this is an improvement. The above change was made so that one continuous simulation, rather of several flat segments, could be used to estimate and visualize the metallurgical length in a curved strand. Predicting the metallurgical length in a more realistic manner is possible when the slab's curvature is taken into account.

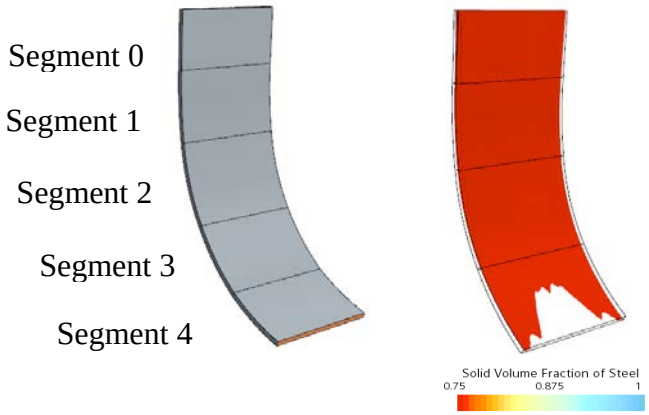

Figure 5-7: Solidification simulation model.

5.2.1 Shell Thickness

An analysis for shell growth behavior was studied along the curved caster. Two positions were taken into consideration given the shell growth behavior shown in figure 5-8. Metallurgical length elongates as shell thickness is monitored away from the centerline and towards the narrow face. Such behavior can be attributed to the cooling distribution profile that allows for faster solidification around the centerline and a slower solidification away from the centerline and towards the narrow face.

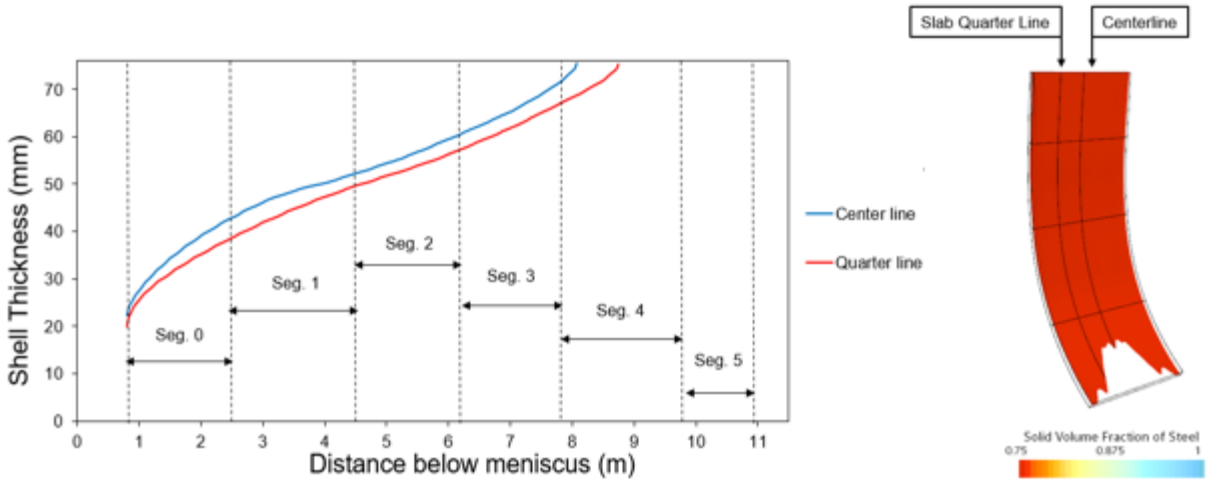

Figure 5-8: Shell Growth and metallurgical length prediction

5.2.2 Temperature

Temperature behavior was analyzed along the caster on three different positions. Centerline and Quarter line like the one used for analyzing as well as inside the slab center, for the purpose of monitoring the liquidus and solidus temperatures. Hence, Figure 5-9 shows a combination of plots that tell three stories about steel behavior as it is being cooled during the secondary cooling phase. A lower surface temperature at centerline can be shown which indicates a higher cooling rate than that of which can be monitored at quarter line, which also coincides perfectly with the results concluded from Figure 5-8 that tells the behavior of shell thickness. At slab center, temperature was also monitored to show how a transitioning from liquidus phase to solidus phase was achieved as cooling was taking place, as such an indication is the primary definition of steel being solidified, specifically inside the slab center.

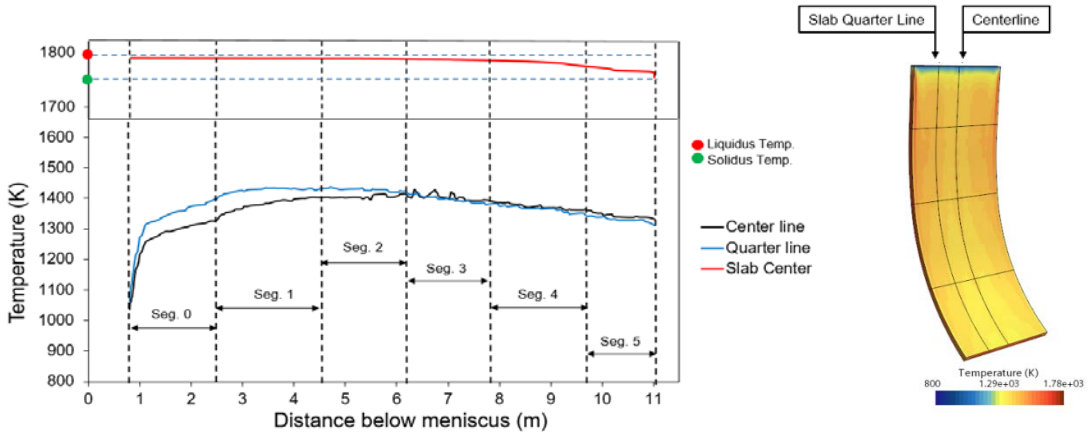

Figure 5-9: Surface and slab center temperature Distribution

5.2.3 Flow effect

It can clearly be seen through Figures 5-10 and 5-11 that high velocities of liquid steel can impact the cooling rate, specifically towards the narrow face at the beginning of the slab. Such phenomenon is a result of the flow shape that is happening in the mold area after steel is being injected from the SEN. Hence, the flow's shape can be altered by making adjustments to the caster's breadth or by installing an EMBr, leading to more uniform cooling and shell growth.

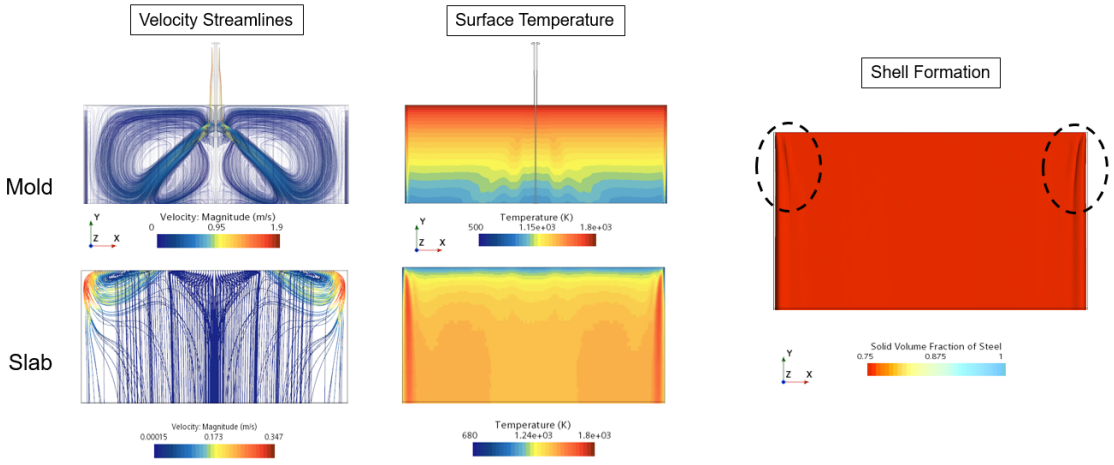

Figure 5-10: Flow field effect on temperature and shell formation

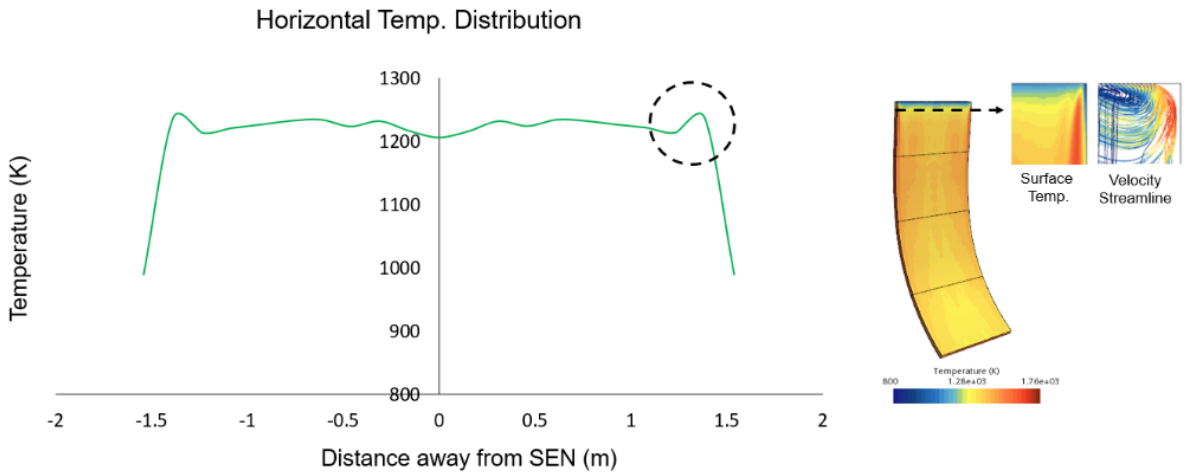

Figure 5-11: Temperature horizontal analysis

5.2.4 Solid volume fraction of steel

A multi-cross sectional view of the solidification process was also extracted to monitor the shell growth and its distribution along the caster. Eventually, all data tells the difference in cooling rate along the caster and as previously mentioned the causes of such differences. Figure 5-12 illustrates the aforementioned description by using the solid volume fraction of steel contour as way to show the distribution of solid, mushy and liquid zones of steel along the caster.

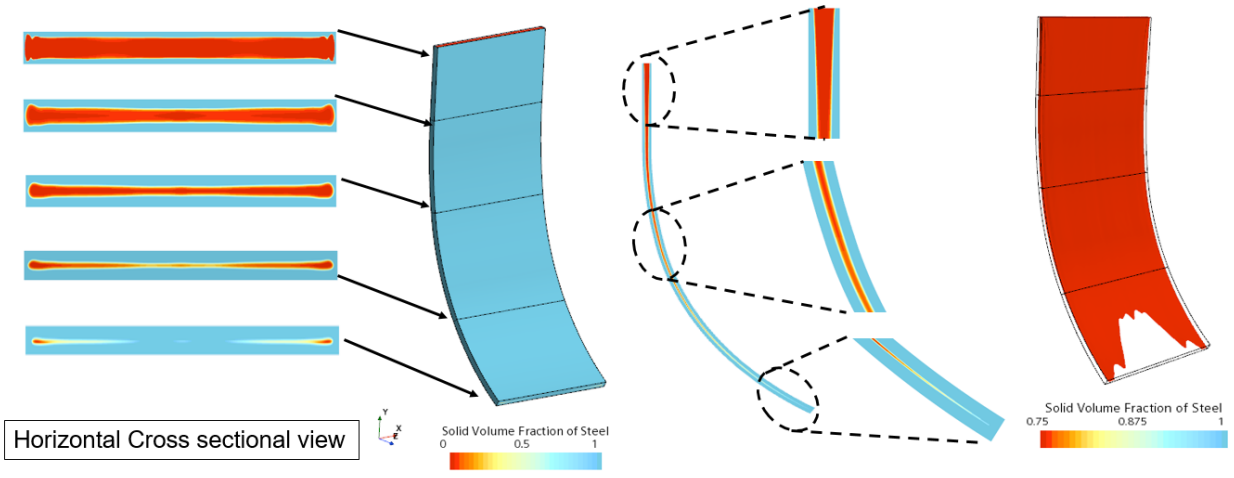

Figure 5-12: Solid volume fraction of steel distribution

5.3 Integration model

5.3.1 Effect of Nozzle Clogging & Casting Speed (Parametric Studies)

The clogging of one and two rows of sprays was achieved by editing the aforementioned spray mapping code such that an edit of the values needed to make the clogging possible is achieved. Clogging initially took place in the shape of “row clogging” as a bulk of sprays altogether and then analyzed at specific places to see the effect of it. Figure 5-18 shows the difference that occurred to the boundary condition due to clogging the nozzles, shape difference is due to each segment having a different arrangement.

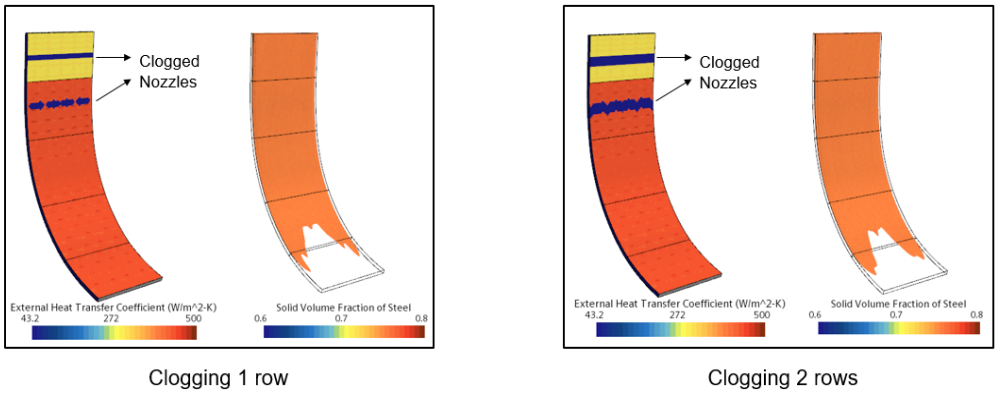

Figure 5-13: Nozzle clogging on the boundary condition

Shell Thickness analysis shows minor differences from baseline case and a positive correlation between nozzles clogged and metallurgical length is found. The more nozzles are clogged, the higher the metallurgical length is. Figure 5-19 show the previously mentioned behavior, with a baseline metallurgical length of 8.25 m.

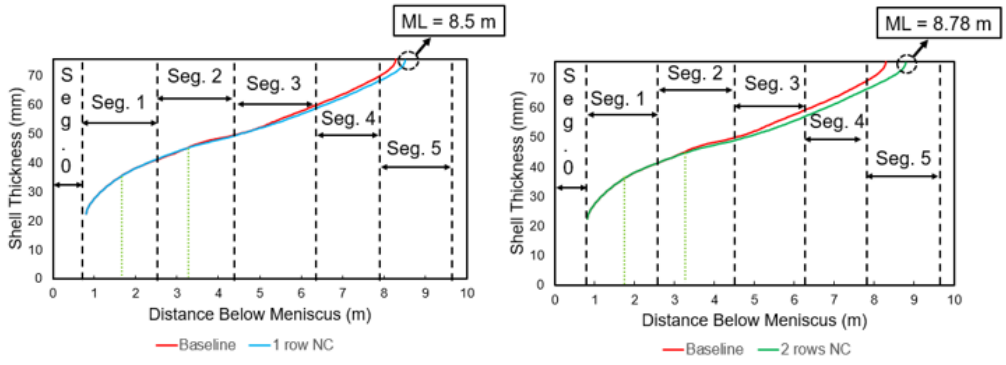

Figure 5-14: One row of nozzle clogging (Left) Two rows of nozzle clogging (Right)

Surface temperature analysis shows that overall cooling is reduced by the nozzle clogging phenomenon, surface temperature rises at the location of the clogged nozzles and another positive correlation between nozzles clogged and surface temperature is further concluded. Figures 5-21 show the previously mentioned behavior and the difference in temperature peaks as well as their incline and decay at the positions of nozzle clogging.

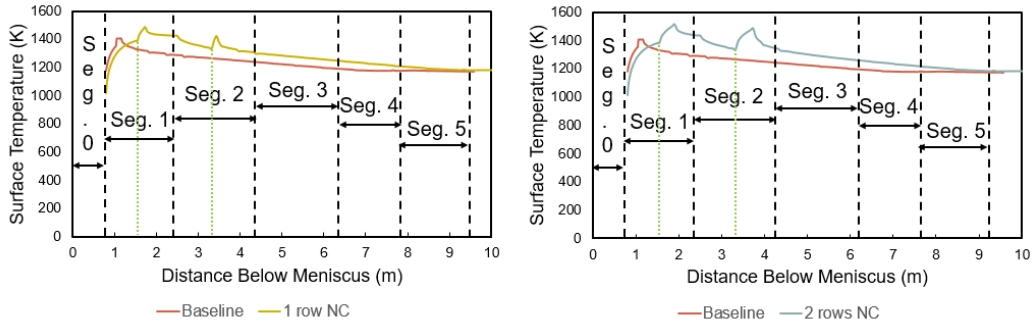

Figure 5-15: Nozzle clogging effect on surface temperature

The data presented in Figure 5-23 elucidate on the influence that increasing casting speed has on metallurgical length. A positive correlation is seen between increasing casting speed and metallurgical length. The metallurgical length tends to increase in direct proportion to the casting speed.

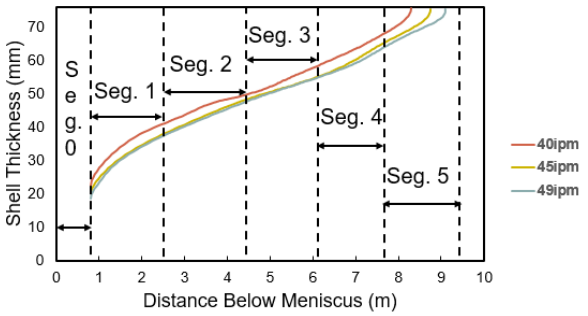

Figure 5-16: Casting speed effect on metallurgical length

6. CONCLUSIONS

Utilizing a three-dimensional computational fluid dynamics simulation, the study examined spray cooling by a flat-fan nozzle during the secondary cooling in continuous steel casting. The findings indicate that the steel continuous casting circumstances have an effect on heat transmission. The heat transfer coefficient under various casting conditions, including water flow rate, casting speed, spray angle, spray overlap, and standoff distance, has been predicted using a new mapping technique. The findings of this study allow for the following inferences:

- The air mist spray simulation uses a 4-step technique and produces higher-resolution results "per spray," but it is computationally expensive, especially if several spray scenarios are needed. The flat fan atomizer model produces above-average quality, but not as high as the first approach. Yet, it has a cheap computing cost and can help when several simulation scenarios and a parallel spraying simulation method are needed.
- Among the three overlap scenarios (3.5%, 12.5%, and 25%), 12.5% overlap was shown to be the best condition for uniform cooling. Under the condition of horizontal overlap, all of which (Nozzle to Nozzle adjustments).
- For the dispersion of the spray arrangement along the caster, a total of 9 distinct spray combinations were used. Water flow rate, spray angle, and stand-off distance were the three factors that were used to create the nine possible combinations.
- In general, a holistic description of cooling was that it is relatively constant on all places at the first segment, then increased gradually and at different stand-offs, gradually decreased some more in the middle, and then concentrates more towards the center of the slab and less towards the edges.

Also, the solidification of steel was examined in order to study certain parameters and how they influence the growth of the shell and the temperature of the surface. The outcome of the spray cooling was incorporated into the solidification model, and an approach to simulation was developed in order to simulate the entire caster. This was done in order to make accurate predictions regarding the shell growth, metallurgical length, and surface temperature of the steel slab. The following hypotheses can be derived from the findings of this study:

- Since the solidification model now accounts for caster strand curvature. Instead of many flat segments, one continuous simulation was used to estimate and display the metallurgical length in a curved strand. The slab's curvature helps predict the metallurgical length in a more realistic and precise manner.
- An analysis for the shell thickness, surface and core temperature, flow formation and solid volume fraction of steel utilizing the new curved caster was conducted and in a smarter, faster and more efficient approach. Rendering the facilitation of such a design the better approach for running secondary cooling simulations.
- The metallurgical length and the number of clogged nozzles are found to be positively correlated by the integration model between the spray simulations, their mapping, and the solidification model. The relationship between surface temperature and clogged nozzles is the same. It is also determined that casting speed and metallurgical length correlate similarly.

7. FUTURE WORKS

Further research will examine the impact of individual nozzle obstruction as well as further overlap tests under various sets of circumstances. Also, given that the code is accessible, any necessary distribution might be created utilizing the HTC database and simulation results for 2D and 3D mapping. The bend along the caster would be employed for additional research for the solidification model, and a wider facilitation of such a model would occur. The impact of solidification rates on the prediction of the metallurgical length would also be investigated further. A database may be created from the simulation of several cases at various casting conditions and for various steel grades, and from there, a correlation could be created to predict the metallurgical length from the composition of the steel, the casting speed, and the superheat. Lastly, due to the remodeling and integration of all models, a wider range of applications and the effects of additional casting circumstances are possible.

REFERENCES

[1] Laitinen, E.; Neittaanmaaki, P. On Numerical Simulation of the Continuous Casting Process. J. Eng. Math. 2003, 22, 335–354.

[2] Thomas, B.G. Continuous Casting (metallurgy). In *Yearbook of Science and Technology*; McGrow-Hill Co.: New York, NY, USA, 2004.

[3] Stahl: World Steel Production. 2009. Available online: http://www.stahlonline.de/english/business_and_politics/economic_and_trade_policy/steel_in_figures/start.asp (accessed on day 02-13-2020).

[4] "From steel to semi-finished products – tec-science", tec-science. [Online]. Available: https://www.tec-science.com/material-science/steel-making/steel-semi-finished-products-continuous-ingot-casting/ [Accessed: 14-Nov-2019].

[5] Camporredondo, S.J.E.; Castillejos, E.A.H.; Acosta, G.F.A.; Gutie'rrez, M.E.P.; Herrera, G.M.A. Analysis of Thin-Slab Casting by the Compact-Strip Process: Part I. Heat Extraction and Solidification. *Metall. Mater. Trans. B* **2004**, *35*, 541–559.

[6] Hibbins, S.G.; Brimacombe, J.K. Characterization of heat transfer in the secondary cooling system of a continuous slab caster. *ISS Trans*. **1983**, *3*, 77–89.

[7] Shiro, N. (1984). The maximum and minimum values of the heat Q transmitted from metal to boiling water under atmospheric pressure. International Journal of Heat and Mass Transfer, 27(7), 959-970.

[8] Agrawal, C. (2019). Surface quenching by jet impingement-a review. Steel Research International, 90(1), 1800285.

[9] Mozumder, A. K., Monde, M., & Woodfield, P. L. (2005). Delay of wetting propagation during jet impingement quenching for a high temperature surface. International Journal of Heat and Mass Transfer, 48(25-26), 5395-5407.

[10] Weigand, B., & Spring, S. (2011). Multiple jet impingement-a review. Heat Transfer Research, 42(2), 101-142.

[11] Ma, H., Silaen, A. K., & Zhou, C., Q. (2020). Numerical development of heat transfer coefficient correlation for spray cooling in continuous casting. Frontiers in Materials, 7, 397.

[12] Mosayebidorcheh, S., & Gorji-Bandpy, M. (2017). Solidification and thermal performance analysis of the low carbon steel during the continuous casting process. Journal of Advanced Materials and Processing, 5(3), 3-11

[13] Sengupta, J., Thomas, B. G., & Wells, M. A. (2005). The use of water cooling during the continuous casting of steel and aluminum alloys. Metallurgical and Materials Transactions A, 36(1), 187-204.

[14] Mundo, C., Tropea, C., and Sommerfeld, M. (1997). Numerical and experimental investigation of spray characteristics in the vicinity of a rigid wall. Exp. Therm. Fluid Sci. 15 (3), 228–237. doi:10.1016/S0894-1777(97)00015-0

[15] Zuckerman, N., and Lior, N. (2006). Jet impingement heat transfer: physics, correlations, and numerical modeling. Adv. Heat Tran. 39, 565–631. doi:10. 1016/S0065-2717(06)39006-5

[16] Rayleigh, L. (1878). On the instability of jets. Proc. Lond. Math. Soc. 1–10 (1), 4–13. doi:10.1112/plms/s1-10.1.4

[17] Weber, C. (1931). Zum Zerfall eines Flüssigkeitsstrahles. Z. Angew. Math. Mech. 11 (2), 136–154. doi:10.1002/zamm.19310110207

[18] O'Rourke, P. J. (1981). Collective drop effects on vaporizing liquid sprays. PhD dissertation. Princeton (NJ): Princeton University.

[19] Liu, A. B., Mather, D., and Reitz, R. D. (1993). Modeling the effects of drop drag and breakup on fuel sprays. J. Engines 102 (3), 83–95. doi:10.4271/930072

[20] Gosman, A. D., and loannides, E. (1983). Aspects of computer simulation of liquidfueled combustors. J. Energy 7 (6), 482–490. doi:10.2514/3.62687

[21] Ranz, W. E., and Marshall, W. R. (1952). Evaporation from drops. Chem. Eng. Prog. 48 (3), 141–146

[22] O'Rourke, P. J. (1981). Collective drop effects on vaporizing liquid sprays. PhD dissertation. Princeton (NJ): Princeton University.

[23] Naber, J. D., and Reitz, R. D. (1988). Modeling engine spray/wall impingement. J. Engines 97 (6), 118–140.

[24] Laitinen, E., and Neittaanmäki, P. (1988). On numerical simulation of the continuous casting process. J. Eng. Math. 22 (4), 335–354. doi:10.1007/BF00058513

[25] Sengupta, J., Thomas, B. G., and Wells, M. A. (2005). The use of water cooling during the continuous casting of steel and aluminum alloys. Metall. Mater. Trans. 36 (1), 187–204. doi:10.1007/s11661-005-0151-y

[26] J. K. Brimacombe and K. Sorimachi, "Crack formation in the continuous casting of steel," *Metall. Trans. B*, vol. 8, no. 2, pp. 489–505, 1977.

[27] F. R. Camisani-Calzolari, I. K. Craig, and P. C. Pistorius, "A review on causes of surface defects in continuous casting," in *IFAC Proceedings Volumes (IFAC-PapersOnline)*, 2003, vol. 36, no. 24, pp. 113–121.

[28] S. Yu *et al.*, "Stress and Friction Distribution around Slab Corner in Continuous Casting Stress and Friction Distribution around Slab Corner in Continuous Casting Mold with Different Corner Structures," *Metall. Mater. Trans. B*, vol. 49, no. 3, pp. 866–876, 2018.

[29] Metzner AB (1985) Rheology of Suspensions in Polymeric Liquids. J. Rheol. New York, New York. vol. 29, no. 6:739–775

[30] Carman PC (1997) Fluid flow through granular beds, Chem. Eng. Res. Des., vol. 75:S32–S48.

[31] Thomas, B. G., & Stone, D. (1998). Measurement of temperature, solidification, and microstructure in a continuous cast thin slab. Retrieved from CiteSeer^{X}

[32] J.K. Brimacombe, Crack formation in Continuous Casting of Steel, Continuous Casting, vol. 2, Iron & Steel Society of AIME, 410, Commonwealth Drive, Warrendale, PA 15086, p. 119–227.

[33] M.M. Wolf, Strand cast halfway cracks — how to read a sulphur print, ISS Steelmaking Conference Proceedings 82 (1999) 3–10.

[34] Thomas, B. G., O'Malley, R., Shi, T., Meng, Y., Creech, D., & Stone, D. (2000, August). Validation of fluid flow and solidification simulation of a continuous thin-slab caster. *Proceedings of Modeling of Casting, Welding, and Advanced Solidification Processes IX*, 20, 25. Aachen, Germany: Shaker Verlag GmbH.

[35] Raudensky, M.; Horsky, J. Secondary cooling in continuous casting and Leidenfrost temperature effects. *Ironmak. Steelmak.* **2005**, *32*, 159–164. https://doi.org/10.1179/174328105X15913.

[36] Thomas, B.G. Continuous Casting of Steel. Chapter 15 in Modeling for Casting and Solidification Processingx, New York, NY, 2001, pp. 499-540.

[37] M.M. Wolf: Continuous Casting: Initial Solidification and Strand Surface Quality of Peritectic Steels, Iron and Steel Society, Warrendale, PA, 1997, vol. 9, pp. 1–111.

[38] Mishra, P.C.; Nayak, S.K.; Pradhan, P.; Durga, P.G. Impingement Cooling of Hot Metal Strips in Runout Table—A Review. *Interfac. Phenom. Heat Transfer* **2015** *Vol. 3*, page 117-137 DOI: 10.1615/InterfacPhenomHeatTransfer.2014010574.

[39] Bryan Petrus, Kai Zheng, X. Zhou, Brian Thomas, Joseph Bentsman. Real-Time, Model-Based Spray-Cooling Control System for Steel Continuous Casting.

[40] K. Okuno, H. Naruwa, T. Kuribayashi, and T. Takamoto: Iron Steel Eng., 1987, vol. 12 (4), pp. 34–38.

[41] K.-H. Spitzer, K. Harste, B. Weber, P. Monheim, and K. Schwerdtfeger: ISIJ Int., 1992, vol. 32 (7), pp. 848–56.

[42] S. Barozzi, P. Fontana, and P. Pragliola: Iron Steel Eng., 1986, vol. 11, pp. 21–26.

[43] B. Lally, L. Biegler, and H. Henein: Metall. Trans. B, 1990, vol. 21B, pp. 761–70.

[44] A. Diener, A. Drastik: Archiv Eisenhu¨ttenwesen, 53 (1982), No 1, 13–20.

[45] B. Barber, B. Patrick, P. Watson, R. York, F. Kitching, H. Sha, K. Kraushaar, K. H. Spitzer: Revue de Metallurgie-CIT, 92 (1996), 1403–1412.

[46] R. Davies, N. P. Blake: Campbell: 4th Int. Continuous Casting Conference, Brussels (1988), 645–654.

[47] Menter FR (1994) Two-equation eddy-viscosity turbulence models for engineering applications. AIAA J., vol. 32, no. 8:1598–1605

[48] Crowe, C.T.; Sharma, M.P.; Stock, D.E. The Particle-Source-In Cell (PSI-CELL) Model for Gas-Droplet Flows. *J. Fluids Eng.* **1977**, *99*, 325–332.

[49] Zuckerman, N.; Lior, N. Jet impingement heat transfer: physics, correlations, and numerical modeling. *Adv. Heat Transfer* **2006**, *39*, 565.

[50] Menter, F.R. Multiscale model for turbulent flows In Proceedings of the AIAA 24th Fluid Dynamics Confernce, Orlando, FL, USA, 6–9 July 1993.

[51] Thomas BG (2018) Intro to Continuous Casting - CCC - U of I. Continuous Casting Consortium. http://ccc.illinois.edu/introduction/basicphenom.html

[52] Thomas BG (2005) Modeling of Continuous-Casting Defects Related to Mold Fluid Flow. *AIST - 3rd Internat. Congress on Science & Technology of Steelmaking*, vol. 3, no. 7, pp. 847–861.

[53] Thomas BG (2003) Chapter 14 – Fluid Flow in the Mold. In: AISE Steel Foundation, Pittsburg, Pennsylvania

[54] Ma, Haibo. ON HEAT TRANSFER MECHANISMS IN SECONDARY COOLING OF CONTINUOUS CASTING OF STEEL SLAB. Diss. Purdue University Graduate School, 2021.

[55] Numerical investigation of air-mist spray cooling and solidification in the secondary zone during continuous casting“ by Vitalis Anisiuba

[56] Numerical Development of Heat Transfer Coefficient Correlation for Spray Cooling in Continuous Casting, Haibo Ma, Armin Silaen and Chenn Zhou, Center for Innovation through Visualization and Simulation (CIVS), Mechanical and Civil Engineering, Purdue University Northwest, Hammond, IN, United States.

[57] Liu, A.B.; Mather, D.; Reitz, R.D. Modeling the Effects of Drop Drag and Breakup on Fuel Sprays. SAE Int. J. Eng. 1993, 102, 83–95.

[58] Ranz, W.E.; Marshall, W.R. Evaporation from Drops. Chem. Eng. Progress 1952, 48, 141–146.

[59] Ishii, M. Thermo-fluid Dynamics Theory of Two-phase Flow. Eyrolles Paris 1975, 75, 29657.

[60] Araki, K.; Moriyama, A. Theory on Deformation Behaviour of a Liquid Droplet Impinging onto Hot Metal Surface. Trans. ISIJ 1981, 21, 583–590.

[61] Bernardin, J.D.; Mudawar, I. The Leidenfrost point: Experimental study and assessment of existing models. J. Heat Trans. 1999, 121, 894–903. https://doi.org/10.1115/1.2826080.

[62] Miller, R.S.; Harstad, K.; Bellan, J. Evaluation of Equilibrium and Non-Equilibrium Evaporation Models for Many Droplet Gas-Liquid Flow Simulations. Int. J. Multiphase Flow 1998, 24, 1025–1055.